Parameterizing an aeolian erosion model for rangelands

Brandon L. Edwards [a,b,*], Nicholas P. Webb [a,b], Magda S. Galloza [a], Justin W. Van Zee [a], Ericha M. Courtright [a], Brad F. Cooper [a], Loretta J. Metz [c], Jeffrey E. Herrick [a], Gregory S. Okin [d], Michael C. Duniway [e], John Tatarko [f], Negussie H. Tedala [g], Daniel N. Moriasi [h], Beth A. Newingham [i], Frederick B. Pierson [j], David Toledo [k], R. Scott Van Pelt [l]

[a] USDA-ARS Jornada Experimental Range, Las Cruces, NM 88003, USA
[b] Plant and Environmental Sciences, New Mexico State University, Las Cruces, NM 88003, USA
[c] USDA-NRCS Resource Assessment Branch, CEAP Grazing Lands, Tucson, AZ 85721, USA
[d] Department of Geography, University of California Los Angeles, Los Angeles, CA 90095, USA
[e] U.S. Geological Survey, Southwest Biological Science Center, Moab, UT 84532, USA
[f] USDA-ARS Rangeland Resources and Systems Research Unit, Fort Collins, CO 80526, USA
[g] US Department of the Interior-BLM, San Luis Valley Field Office, Monte Vista, CO 81144, USA
[h] USDA-ARS USDA-ARS Grazinglands Research Laboratory, El Reno, OK 73036, USA
[i] USDA-ARS Great Basin Rangelands Research Unit, Reno, NV 89512, USA
[j] USDA-ARS Northwest Watershed Research Center, Boise, ID 83702, USA
[k] USDA-ARS Northern Great Plains Research Laboratory, Mandan, ND 58554, USA
[l] USDA-ARS Wind Erosion and Water Conservation Unit, Big Spring, TX 79720, USA

ABSTRACT

Aeolian processes are fundamental to arid and semi-arid ecosystems, but modeling approaches are poorly developed for assessing impacts of management and environmental change on sediment transport rates over meaningful spatial and temporal scales. For model estimates to provide value, estimates of sediment flux that encapsulate intra- and inter-annual and spatial variability are needed. Further, it is important to quantify and communicate transparent estimates of model uncertainty to users. Here, we present a wind erosion and dust emission model parameterized for rangelands using a Generalized Likelihood Uncertainty Estimation framework. Modeled horizontal sediment flux was calibrated using data from five diverse grassland and shrubland sites from the USDA National Wind Erosion Research Network. Observations of wind speed, vegetation height, length of gaps between vegetation, and percent bare ground were used as model inputs. Horizontal sediment flux estimates from 10,000 independently selected parameter sets were compared to flux observations from 44 ~ month-long collection periods to calculate a likelihood measure for each model. Results show good agreement for individual sampling periods across sites with few observations falling outside prediction bounds and a one-to-one relationship between median predictions and observations. Additionally, combined distributions of sediment flux estimates from all sample periods for a given site closely approximated the probability of observing a given flux at that site. These results suggest AERO effectively represents temporal variability in aeolian transport rates at rangeland sites and provides robust assessments suitable for assessing land health and better predicting changes in air quality and the impacts of land management activities.

Introduction

Aeolian processes play a fundamental role in dryland ecosystems and how they respond to disturbance, land use, and environmental change (Ravi et al., 2011; Webb et al., 2020a). Soil erosion and nutrient redistribution by wind can impact soil health, biogeochemical cycles, plant productivity, and ecosystem resilience (Okin et al., 2015; Webb et al., 2017). Soil deflation, root exposure, and plant tissue damage occur during extreme wind events and can result in mortality of perennial grasses and other herbaceous species (Alvarez et al., 2012; Gonzales et al., 2017). During more frequent, lower-intensity sediment transport events, many shrubs capture blowing soil and nutrients, which promotes

species composition change and loss of ecosystem services (Schlesinger et al., 1990; Bestelmeyer et al., 2018). Dust emissions impact climate (Mahowald et al., 2014), air quality (Achakulwisut et al., 2017), and human health (Goudie, 2014), while episodic dust storms directly threaten human life, infrastructure, and material resources (Pimentel et al., 1995; Middleton, 2017). Quantifying the frequency, timing, and magnitude of wind erosion and dust emission—and interpreting associated costs and risks—is thus critical for managing local and downwind impacts (Edwards et al., 2019; Webb et al., 2020a). Despite broad recognition of these needs among researchers and land managers, there is a lack of consistent, actionable information and tools that can support dryland wind erosion management (Webb et al., 2020b).

Cropland wind erosion models have successfully been adopted by agencies globally to support soil conservation planning and identify potential impacts of land use and management strategies on soil loss and deposition, fine dust emissions (i.e., PM2.5 & PM10), and air quality (e.g., Tatarko et al., 2019; Jarrah et al., 2020). Such models have yet to be extended to rangelands, however, because parameterization for mixed plant community structures, diverse landscapes, and disturbance is difficult (Li et al., 2014). In the United States (US), Environmental Protection Agency (EPA) empirical emissions factors are used by rangeland managers to assess potential impacts of some land uses on particulate matter (PM) emissions (EPA, 2018), but the utility of this approach is limited because emissions factors are explicitly linked to narrowly defined, mostly industrial activities. Process-based emission models have been developed to forecast air quality and assess dust effects on climate (Haustein et al., 2015), but also have limited utility for informing dryland management (Webb and McGowan, 2009). Model validation using offsite dust concentrations and reliance on preferential dust source functions (e.g., Ginoux et al., 2001; Parajuli et al., 2019) largely preclude using these models to assess *why* landscapes are eroding. Ascribing contributing factors to erosion is important for rangelands, where land uses like livestock production, energy development, recreation, and land management activities are strongly linked with aeolian processes (Duniway et al., 2019). Applications of wind erosion and dust emission models at fine scales have demonstrated their potential for understanding management effects (e.g., Pierre et al., 2018), but further work is needed to improve model accuracy and sensitivity to diverse soils and heterogeneity in the cover, structure, and composition of vegetation.

Without robust models, current rangeland wind erosion assessment relies on qualitative methods that describe evidence of historical wind erosion (e.g., Herrick et al., 2019; Pellant et al., 2020) and interpretation of soil and vegetation indicators that indirectly describe current erosion risk (Herrick et al., 2018; Webb et al., 2020b). Developing the capacity to quantitatively assess indicators of wind erosion and dust emission would complement these approaches (Webb et al., 2020b). Making models and quantitative indicators available to land managers would encourage more integrated approaches to dryland management that consider land health and air quality impacts of wind erosion alongside other ecosystem attributes (e.g., Herrick et al., 2010; Toevs et al., 2011). Some quantitative rangeland and pastureland monitoring programs already collect soil and vegetation data using standard monitoring methods (Herrick et al., 2018) and remote sensing (e.g., Jones et al., 2018; Zhang et al., 2019; Zhou et al., 2020) that could enable accurate, quantitative estimates of sediment transport and dust emission (Webb et al., 2017). In the US, the Natural Resources Conservation Service's (NRCS) grazing lands National Resources Inventory (NRI), Bureau of Land Management's (BLM) Assessment, Inventory and Monitoring (AIM) program, National Park Service's (NPS) Inventory and Monitoring (I&M) program, and other government agency programs have implemented core monitoring methods from Herrick et al. (2018) at over 65,000 monitoring locations on federal and non-federal lands since 2004. Data collected by these programs support quantitative indicators of ground cover, vegetation height, the size distribution of unvegetated gaps between plants, and soil surface properties. These indicators could enable more accurate quantification of landscape susceptibility to wind erosion and incorporation of wind erosion information into existing land health and air quality assessment approaches (e.g., Kachergis et al., 2020), but a new modeling approach is needed that can leverage these data to develop new indicators of wind erosion and dust emission at scales meaningful for dryland management.

Here, we present the Aeolian EROsion (AERO) model with parameterization of horizontal sediment flux for rangelands. AERO integrates established physical models (e.g., Kawamura, 1951; Shao and Lu, 2000; Shao, 2004; Okin, 2008) of the key components of aeolian sediment transport systems to predict particle size-resolved streamwise horizontal sediment flux Q (kg m^{-1} s^{-1}) and vertical dust emission F (kg m^{-2} s^{-1}). We calibrated AERO using observations of standardized vegetation monitoring data, meteorological conditions, and horizontal sediment flux from five grassland and shrubland sites from the National Wind Erosion Research Network (NWERN) in the western US using the Generalized Likelihood Uncertainty Estimation (GLUE) approach (Beven and Binley, 1992). The GLUE approach explicitly recognizes model equifinality—there are many possible combinations of parameter values for a given model that produce suitable solutions—and accounts for unknown sources, structure, and magnitude of errors among component models, variables, and observations. GLUE also enables reporting of weighted distributions of model predictions that provide a more holistic view of sediment transport rates that could be expected at a site and support risk-based interpretations, where it is useful to understand the range and probability of possible outcomes. Results suggest that AERO appropriately describes aeolian sediment transport dynamics and provides necessary information to enhance current land health and air quality assessments through development of meaningful wind erosion indicators and management benchmarks for rangelands.

Description of AERO model

AERO is a largely physically-based aeolian sediment transport and dust emission modeling scheme developed to leverage standardized ecological monitoring data to produce plot-scale estimates of Q and F. AERO estimates Q based on surface soil particle size distribution, wind speed, and vegetation cover and structure. F is estimated based on surface soil particle size distribution, wind speed, and Q and includes expressions for saltation bombardment and soil disaggregation following Shao (2004). Q and F are reported per unit width (of a vertical plane intersecting the surface and perpendicular to the direction of transport) and unit surface area, respectively. Thus, there is no prescribed spatial extent constraining flux estimates. The ecological monitoring data that AERO was developed to leverage typically describe conditions over plots on the order of 1 ha, but AERO could also be implemented to represent transport at a single point or over a larger area—assuming relevant controls remain within acceptable limits.

The model employs a core set of generalizable, mechanistic functions representing fundamental aeolian processes that operate over either scalar values or probabilistic representations of key variables Fig. 1. As such, AERO is flexible in that it can produce sediment flux estimates from minimal inputs—e.g., for a single wind speed and sediment transport threshold in the absence of vegetation—yet is designed to implement the most fully realized simulation possible given the level of available information. The equations presented here represent the full implementation of AERO for standardized rangeland monitoring data. Required model inputs include bare ground cover fraction, mean vegetation height, surface soil particle size distributions (PSDs), unvegetated canopy gap length observations, and wind speed observations (or distribution parameters). Model parameters used to calibrate AERO estimates of Q for rangelands are identified in the following description. The dust emission scheme is presented in deference to completeness but has not yet been parameterized in AERO.
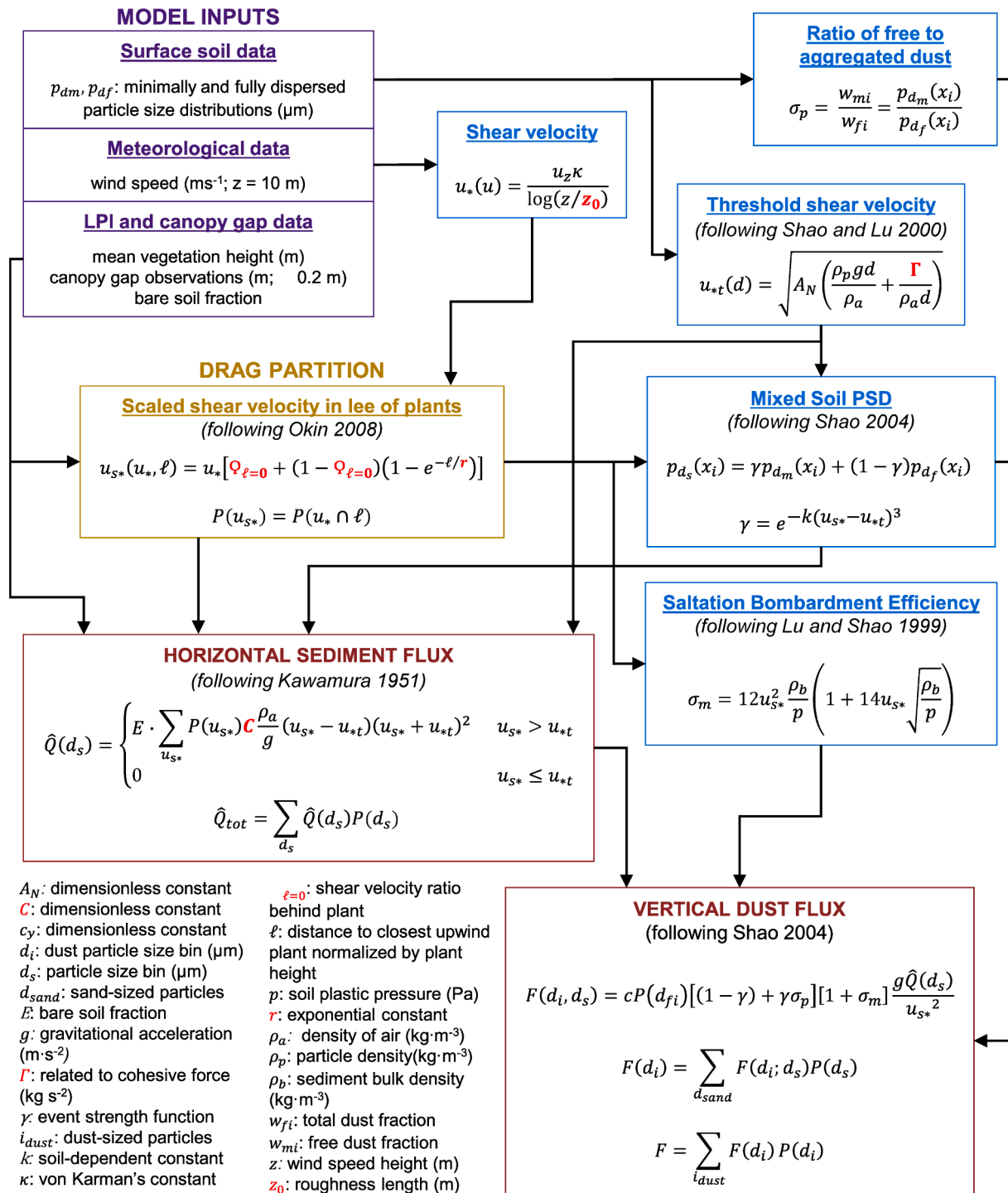
MODEL INPUTS

Surface soil data

p_{dm}, p_{df}: minimally and fully dispersed particle size distributions (µm)

Meteorological data

wind speed (ms^{-1}; z = 10 m)

LPI and canopy gap data

mean vegetation height (m)
canopy gap observations (m; 0.2 m)
bare soil fraction

Shear velocity

$$u_*(u) = \frac{u_z \kappa}{\log(z/z_0)}$$

Ratio of free to aggregated dust

$$\sigma_p = \frac{w_{mi}}{w_{fi}} = \frac{p_{d_m}(x_i)}{p_{d_f}(x_i)}$$

Threshold shear velocity
(following Shao and Lu 2000)

$$u_{*t}(d) = \sqrt{A_N \left(\frac{\rho_p g d}{\rho_a} + \frac{\Gamma}{\rho_a d} \right)}$$

DRAG PARTITION

Scaled shear velocity in lee of plants
(following Okin 2008)

$$u_{s*}(u_*, \ell) = u_* \left[Q_{\ell=0} + (1 - Q_{\ell=0})(1 - e^{-\ell/r}) \right]$$

$$P(u_{s*}) = P(u_* \cap \ell)$$

Mixed Soil PSD
(following Shao 2004)

$$p_{d_s}(x_i) = \gamma p_{d_m}(x_i) + (1 - \gamma) p_{d_f}(x_i)$$

$$\gamma = e^{-k(u_{s*} - u_{*t})^3}$$

Saltation Bombardment Efficiency
(following Lu and Shao 1999)

$$\sigma_m = 12 u_{s*}^2 \frac{\rho_b}{p} \left(1 + 14 u_{s*} \sqrt{\frac{\rho_b}{p}} \right)$$

HORIZONTAL SEDIMENT FLUX
(following Kawamura 1951)

$$\hat{Q}(d_s) = \begin{cases} E \cdot \sum_{u_{s*}} P(u_{s*}) C \frac{\rho_a}{g} (u_{s*} - u_{*t})(u_{s*} + u_{*t})^2 & u_{s*} > u_{*t} \\ 0 & u_{s*} \leq u_{*t} \end{cases}$$

$$\hat{Q}_{tot} = \sum_{d_s} \hat{Q}(d_s) P(d_s)$$

VERTICAL DUST FLUX
(following Shao 2004)

$$F(d_i, d_s) = cP(d_{fi})[(1 - \gamma) + \gamma \sigma_p][1 + \sigma_m] \frac{g \hat{Q}(d_s)}{u_{s*}^2}$$

$$F(d_i) = \sum_{d_{sand}} F(d_i; d_s) P(d_s)$$

$$F = \sum_{i_{dust}} F(d_i) P(d_i)$$

A_N: dimensionless constant
C: dimensionless constant
c_y: dimensionless constant
d_i: dust particle size bin (µm)
d_s: particle size bin (µm)
d_{sand}: sand-sized particles
E: bare soil fraction
g: gravitational acceleration (m·s^{-2})
Γ: related to cohesive force (kg s^{-2})
γ: event strength function
i_{dust}: dust-sized particles
k: soil-dependent constant
κ: von Karman's constant

$Q_{\ell=0}$: shear velocity ratio behind plant
ℓ: distance to closest upwind plant normalized by plant height
p: soil plastic pressure (Pa)
r: exponential constant
ρ_a: density of air (kg·m^{-3})
ρ_p: particle density(kg·m^{-3})
ρ_b: sediment bulk density (kg·m^{-3})
w_{fi}: total dust fraction
w_{mi}: free dust fraction
z: wind speed height (m)
z_0: roughness length (m)

Fig. 1. Variables, calculation steps, and component equations of the Aeolian EROsion (AERO) model. Figure shows the full implementation of AERO presented in this paper. Parameters used to calibrate AERO for horizontal sediment flux are shown in red. (For interpretation of the references to color in this figure legend, the reader is referred to the web version of this article.)

Representing a dynamic sediment bed

AERO requires minimally and fully dispersed surface (0–1 cm) soil PSDs $p_{dm}(x)$ and $p_{df}(x)$ to estimate Q and F. If site-specific PSDs are not available, AERO uses a search function to select the closest member in sand–silt–clay percentage space from an internal database of representative soils sampled across the western US (and Australia, if desired).

Following Shao (2004) and Shao et al. (2011), the two distributions represent possible end members of the physical character of the

sediment bed—i.e., before a transport event and assuming complete breakdown of soil aggregates during transport, respectively. For both distributions, particle size bin midpoints x_i are distributed logarithmically such that:

$$x_i = \left(\frac{d_{max}}{d_{min}} \right)^{i-1/n} d_{min} \left(\frac{d_{max}}{d_{min}} \right)^{i/n} d_{min} \right)^{0.5} \tag{1}$$

where $d_{max} = 1000$ µm, $d_{min} = 0.1$ µm, and $n = 200$. AERO assumes that saltating aggregates break apart to some degree upon impact with the

sediment bed during transport. As such, soil PSD $p_{d_s}(x)$ is calculated by a weighted mix of $p_{d_m}(x)$ and $p_{d_f}(x)$ as:

$$p_{d_s}(x_i) = \gamma p_{d_m}(x_i) + (1-\gamma)p_{d_f}(x_i) \, for \, all \, x_i \tag{2}$$

to represent the event-specific sediment bed. The degree to which the distribution moves toward being fully dispersed depends on γ, which represents the relative strength of the event. Lu and Shao (2001) defined γ as:

$$\gamma = e^{-k(u_{s*}-u_{*t})^3} \tag{3}$$

where parameter k describes the rate at which $\gamma \to 0$ as surface shear velocity u_{s*} (m s^{-1}) increases above threshold shear velocity u_{*t} (m s^{-1}), or how easily soil aggregates are broken down during transport. As $\gamma \to 1$, i.e., for weak transport events, soil disaggregation becomes negligible. Conversely, as $\gamma \to 0$ (very strong event),$p_{d_s}(x_i) \to p_{d_f}(x_i)$. It should be noted that: 1) u_{*t} in Eq. (3) is the minimum value of u_{*t} from Eq. (12); and 2) while AERO currently uses a value of $k = 0.5$, Shao et al. (2011) suggest that the value of k is soil dependent. However, Eq. (2) has the largest influence on dust production from aggregates and has negligible impact on particle sizes susceptible to saltation in the model, i.e., where inertial force resisting motion is orders of magnitude larger than inter-granular cohesive force (Edwards and Namikas, 2015). As such, k has not been parameterized in the current effort.

Estimating horizontal sediment flux

Estimated size-resolved saltation flux $\widehat{Q}(d_s)$ is calculated following Kawamura (1951) as:

$$\widehat{Q}(d_s) = \begin{cases} E \cdot \sum_{u_{s*}} P(u_{s*})C\frac{\rho_a}{g}(u_{s*}-u_{*t})(u_{s*}+u_{*t})^2 & u_{s*} > u_{*t} \\ 0 & u_{s*} \le u_{*t} \end{cases} \tag{4}$$

where E is fractional cover of exposed, bare soil (i.e., excluding areas below plant canopies or covered by plant litter and other impediments), ρ_a is fluid density (kg m^{-3}), g is gravitational acceleration (9.81 m s^{-2}), u_{*t} (m s^{-1}) is threshold shear velocity, and C is an unknown dimensionless parameter—originally suggested as related to grain size and sorting (e.g., Kawamura, 1951; Bagnold, 1936)—that relates empirical measurements to theoretical flux rates. $P(u_{s*})$ is the probability of a given shear velocity at the soil surface u_{s*} such that:

$$p_{u_{s*}}(x) = P(u_{s*} = x) \, for \, all \, x \in S \tag{5}$$

where the sample space S is determined by the relative ranges and magnitudes of probability distributions of wind speed u (m s^{-1}) and the size of unvegetated gaps between plants, which modulate the transfer of momentum from the wind to the sediment bed.

First, the wind speed probability distribution:

$$p_u(x) = P(u=x) for \left\{ x_1, x_2, \cdots, x_n | x_i = \frac{i(u_{max}-u_{min})}{n}, \, i = 1, 2, \cdots, n \right\} \tag{6}$$

where $n = 250$, is estimated using *in situ* measurements or pre-estimated wind speed probability distribution parameters for a given location. If *in situ* measurements are used, wind speeds are binned to the closest value of x_i before $P(u=x)$ is calculated. Next, shear velocity for each wind speed from Eq. (6) $u_*(u)$, which assumes a bare surface, is calculated as:

$$u_*(u) = \frac{u_z \kappa}{\log(z/z_0)} \tag{7}$$

where z is the wind speed measurement height (m), z_0 is the aerodynamic roughness length (m), and κ is the von Kármán constant ($\approx$ 0.4). Each $u_*(u)$ is assigned the same probability as $P(u)$. Because Eq. (7) requires z_0—an inherently dynamic function of surface configuration and wind speed—to be fixed across a range of conditions, AERO treats it

as a parameter of unknown value similar to the approach of Li et al. (2013). This approach also has the advantage, within the GLUE calibration framework, of accounting for the interaction between z_0 and C in Eq. (4) in the model parameterization.

AERO implements the drag partition scheme developed in Okin (2008) to describe the effect of vegetation on attenuating momentum transfer from the wind field to the soil surface and the resulting spatial distribution of surface shear stress. Conceptually, the Okin (2008) scheme describes the accumulated effects of the reduction and subsequent recovery of $u_*(u)$ in the lee of individual plants, which has the advantage of treating the problem probabilistically across values of u rather than as a static increase in u_{*t} for all meteorological conditions (e. g., in the commonly implemented Raupach et al. (1993) drag partition). Other major benefits of this approach are: 1) the drag partition scheme can be applied explicitly to *in situ* vegetation conditions using widely available rangeland monitoring data, and 2) it is sensitive to the spatial configuration of vegetation at a site. Thus, AERO is appropriately sensitive to ecosystem changes resulting from land management or other disturbances.

The scheme stipulates that in the lee of a plant, $u_*(u)$ is reduced by ratio φ to $u_{s*}(u_*, \ell)$, the shear velocity at the soil surface as a function of u_* and ℓ—the distance from the closest upwind plant l_p (m) normalized by vegetation height h (m). AERO uses standard monitoring observations (e.g., Herrick et al., 2018) of canopy gap lengths (length of unvegetated gaps between plants) l_g (m) normalized by h to estimate the probability distribution of scaled canopy gap lengths $P(l_g/h)$ such that:

$$p_{(l_g/h)}(x) = P\left((l_g/h) = x\right) for \left\{ x_1, x_2, \cdots, x_n | x_i = \frac{i(l_{gmax}-l_{gmin})}{n}, i \right. $$
$$\left. = 1, 2, \cdots, n \right\} \tag{8}$$

where $n = 100$ and l_{gmin} and l_{gmax} are the minimum and maximum observations of l_g, respectively. In cases where there are less than 100 vegetation gap observations, e.g., for densely vegetated areas or for sparsely vegetated areas with mostly bare interspaces, $x_1, x_2, \cdots, x_n = l_{g1}, l_{g2}, \cdots, l_{gn}$. $p_\ell(x)$ for the same $\{x_1, x_2, \cdots x_n\}$ is then easily estimated because $P(\ell)$ is directly proportional to $P(l_g/h)$ as:

$$P(\ell) \propto \frac{P(l_g/h)}{(l_g/h)} \tag{9}$$

Eq. (9) effectively distributes the probability for a given scaled gap size evenly across the interval $(0, l_g/h]$. Renormalization such that:

$$\sum_{i=1}^{n} p_\ell(x_i) = 1 \tag{10}$$

completes the proportionality. It should be noted that in practice, when using standard rangeland monitoring data, $0.2 \le l_g \le 50$ *or* 100 m, which are the typical minimum gap length reported and transect length for monitoring plots, respectively.

The Okin (2008) drag scheme is then implemented for each $u_*(u)$ as:

$$u_{s*}(u_*, \ell) = u_* \left[\varphi_{\ell=0} + (1-\varphi_{\ell=0})\left(1 - e^{-\ell/r}\right) \right] \tag{11}$$

where $\varphi_{\ell=0}$ is the shear velocity ratio (u_{*s}/u_*) in the immediate lee of a plant and r determines the rate of shear velocity recovery downwind. Data supporting appropriate values of $\varphi_{\ell=0}$ and r are limited in the literature; hence AERO treats both as parameters of unknown value, again similar to Li et al. (2013). Eq. (11) necessarily results in a large number of values of u_{s*} (max of $n = 250 \times n = 100$). Thus, results are binned as they are calculated into $p_{u_{s*}}(x)$ such that successive bin boundaries are at least 0.002 m s^{-1} apart and probabilities $P(u_* \cap \ell)$ are accumulated within each bin.

AERO calculates threshold shear velocity used in Eq. (4) for all x_i in $p_d(x)$ following Shao and Lu (2000) as:

$$u_{*t}(d) = \sqrt{A_N \left(\frac{\rho_p g d_m}{\rho_a} + \frac{\Gamma}{\rho_a d}\right)} \qquad (12)$$

where A_n is a dimensionless coefficient ≈ 0.0123, ρ_p is particle density (kg m^{-3}), and Γ represents the influence of interparticle cohesion. Shao and Lu (2000) suggested that Γ varies between 1.65×10^{-4} and 5×10^{-4}. AERO treats Γ as an unknown parameter. It should be noted that AERO is capable of modifying $u_{*t}(d)$ for soil moisture, e.g., following Fécan et al. (1999), if desirable, but no correction was used here.

Total streamwise sediment flux Q is calculated by summing the contribution for each particle size bin as:

$$\widehat{Q}_{tot} = \sum_{d_s} \widehat{Q}(d_s) P(d_s) \qquad (13)$$

Estimating dust emission

AERO estimates F following Shao (2004). Size-resolved vertical dust emission rate $F(d_i, d_s)$ of particles in the ith size bin d_i resulting from saltation of particles sized d_s is estimated by:

$$F(d_i, d_s) = cP(d_{fi})\left[(1-\gamma) + \gamma\sigma_p\right]\left[1 + \sigma_m\right]\frac{g\widehat{Q}(d_s)}{u_{s*}^2} \qquad (14)$$

where c is a dimensionless fitting coefficient and $P(d_{fi})$ constrains estimates of $F(d_i, d_s)$ to the mass fraction of total available dust in d_{fi}—i.e., the amount of dust emission predicted from d_i cannot exceed the amount from that bin in the fully dispersed soil PSD. σ_p describes the ratio of freely available, non-aggregated dust to total dust in d_i such that:

$$\sigma_p = \frac{w_{mi}}{w_{fi}} = \frac{p_{d_m}(x_i)}{p_{d_f}(x_i)} \qquad (15)$$

The bracketed expressions in Eq. (14) describe dust emission as the combined effect of the breakdown of soil aggregates during transport, emission of free dust particles, and particle ejection caused by saltating particles of a given size impacting the sediment bed. As $\gamma \to 1$, the contribution of soil disaggregation to dust emission becomes negligible, and as γ decreases the contribution of disaggregation increases. As the relative proportion of freely available dust in the sediment bed σ_p increases for a given event strength, the contribution of the emission of free dust increases.

Saltation bombardment efficiency σ_m represents the ratio of the mass of soil ejected by a particle impacting the bed to that particle's mass, and is described by an expression developed by Lu and Shao (1999) simplified for typical particle and bulk densities for silicate soils as:

$$\sigma_m = 12u_{s*}^2\frac{\rho_b}{p}\left(1 + 14u_{s*}\sqrt{\frac{\rho_b}{p}}\right) \qquad (16)$$

where ρ_b is soil bulk density (kg m^{-3}, assumed ≈ 1000') and p is the soil plastic pressure (Pa), which represents how resistant to deformation the soil surface is. For low p, soils are relatively loose and erodible, and the contribution of saltation bombardment to particle ejection is significant. As p increases, the contribution of saltation bombardment to emitted dust decreases until negligible.

Vertical dust flux from d_i generated by saltation of all sand-sized particles in range d_{sand} is estimated as:

$$F(d_i) = \sum_{d_{sand}} F(d_i; d_s) P(d_s) \qquad (17)$$

and total dust flux for dust-sized particles is given by:

$$F = \sum_{i_{dust}} F(d_i) P(d_i) \qquad (18)$$

In AERO, the upper limit of i_{dust} = lower limit of d_{sand} and is user selectable. Suggested ranges of c and p, are $[1, 5] \times 10^{-5}$ and $[1, 50] \times 10^3$

Pa, respectively (Shao, 2004). c, p, and ρ_b will be treated as unknown parameters in AERO when the dust emission scheme is calibrated for rangelands in future efforts.

Methods

A major challenge in developing wind erosion and dust emission models is acquiring robust data across land use and land cover types. Aeolian horizontal sediment flux and dust emission are inherently variable across space and through time. Thus, data networks and reliable observations with explicit recognition of the heterogeneity of physical processes are needed to meet advances in approaches to modeling physical systems (Kirchner, 2006). Drivers of change, controls, and fundamental sediment transport processes occur across scales from instantaneous to geologic and grain-scale to planetary. The number of coincident physical samples needed to detect differences in aeolian sediment flux among ecologically similar sites—or detect change at a single site through time—is prohibitive to most monitoring efforts (Webb et al., 2019). The typical approach to aeolian model parameterization, where models are conditioned using observations from a single location, limited experimental data, or unrelated data parsed from the literature, fails to represent spatiotemporal variability of aeolian processes in a meaningful way for characterizing long-term behavior at a site and informing land management.

The National Wind Erosion Research Network (NWERN) was established in 2014 to support model development, with an emphasis on models parameterized using field data collected following standard protocols (Herrick et al., 2018), and facilitate leveraging large ecosystem monitoring datasets to produce wind erosion assessments across scales (Webb et al., 2016; https://winderosionnetwork.org/). The network currently comprises 18 sites extending from ~32 to 50° N latitude and ~98 to 117° W longitude.

The network collects standardized observations of aeolian sediment transport rates, size-resolved dust emission, and environmental controls and uses a rigorous stratified random sample design to measure spatiotemporal variability in aeolian sediment transport over 1 ha sites (Webb et al., 2016). Network sites employ the same standardized monitoring methods used by federal agencies in the US to monitor and assess the status, condition and trend of grazing lands (Toevs et al., 2011). Field data for model calibration were collected at five NWERN sites in the western United States (Table 1). Sites used to calibrate AERO comprise grasslands and shrublands located in the Chihuahuan Desert, Arizona/New Mexico Plateau, Colorado Plateau, and High Plains Ecoregions that are grazed by livestock and other wildlife (Fig. 2, Table 1). AERO was conditioned against vegetation, surface (0–1 cm) soil PSD, and wind speed measurements (the variable inputs), and 44 ~ 1-month long horizontal sediment flux observation periods (~850 K sampler-hours) across the five sites.

Field measurements

Wind speeds are measured at NWERN sites at heights of 0.5, 1, 1.5, 2.5, 5 and 10 m using RM Young 03101 cup anemometers. Anemometers are sampled at a frequency of 1 Hz frequency and samples are averaged to produce 1-minute average wind speeds. For AERO calibration, only the 10-meter wind speeds were used as model inputs for consistency with available wind speed estimates for monitoring plots that AERO was designed to leverage. For the 8 June 2017 and 5 July 2017 (Table 2) sediment flux observation periods at SLV, 5-meter wind speeds were used instead and the model adjusted accordingly because the 10-meter anemometer required maintenance during that period.

Vegetation and soil surface characteristics were measured following standard NWERN methods along three 100-m transects crossing through the site center. The line-point intercept (LPI) method (Herrick et al., 2018) was used to quantify total foliar and ground cover from which percent bare soil is calculated. Vegetation height was measured every 2

Table 1
Management, ecological, and location information for National Wind Erosion Research Network (NWERN) field sites used to calibrate Aeolian EROsion (AERO) model.

Site ID	JER	HAFB	Moab	SLV	CPER
Site management	USDA-ARS Jornada Experimental Range Long Term Agro-ecosystem Research (LTAR) Network	USDA-ARS Jornada Experimental Range Long Term Agro-ecosystem Research (LTAR) Network	USGS Southwest Biological Science Center	BLM San Luis Valley field office	USDA-ARS Central Plains Experimental Range Long Term Agro-ecosystem Research (LTAR) Network
Location	32.6271−106.7387	32.9423−106.1073	38.6515−109.8696	37.5991−105.6907	40.8349−104.6973
Elevation	1320 m	1267 m	1575 m	2300 m	1650 m
Ecoregion (level III)	Chihuahuan Desert	Chihuahuan Desert	Colorado Plateau	Arizona/New Mexico Plateau	Western High Plains
Surface soil (USDA standard soil texture classes)	Sandy loam to fine sandy loam, weak biological and physical crusting	Gypsiferous fine to very fine sandy loam, strong biological crusting	Loamy fine sands, weak to moderate biological and physical crusting	Sandy soil overlying natric sandy loam to clay loam soils, weak physical and biological crusting	Fine sandy loam overlying sandy clay loams, moderate to strong physical crusting
Land cover	Shrubland	Grassland	Grassland	Shrubland	Grassland

m along each transect to estimate a site mean, and vegetation canopy gap lengths > 5 cm were recorded along each transect (see Webb et al., 2015 for details). Vegetation transect measurements are conducted approximately quarterly at all NWERN sites to capture seasonal and phenological changes.

Surface soil samples were collected from each site using a stratified random sampling design. Three groups of 1-cm deep scoop samples were collected at randomly chosen locations inside each cell in a regular 3x3 grid across the site (27 samples total). Samples were combined to produce three composite samples per site. Samples were sieved to 2 mm maximum size and organic material and litter ≥ 2 cm long and/or 1 mm wide were removed. Soil PSDs were measured using a Beckman Coulter LS 13 320 laser particle size analyzer. Three samples were randomly split out from each composite, and results averaged to produce PSDs for each site. Minimally dispersed samples were analyzed using low power sonification during measurement. Fully dispersed samples were prepared by agitating the sample in a standard 5% solution of sodium hexametaphosphate for ~24 h on a reciprocating shaker table. The sample was further agitated with high power sonication for two minutes prior to and during measurement.

Horizontal sediment flux measurements

NWERN sites use a stratified random sample design with 27 Modified Wilson and Cooke (MWAC) sediment sampler masts to capture spatio-temporal variability of horizontal sediment mass flux. Each mast has samplers at 0.10, 0.25, 0.50 and 0.85 m height. Sites are stratified in a regular 3×3 grid and MWAC masts are located at three random positions within each cell. Samples were collected every ~28 days and weighed to determine sediment mass per sampler (following Webb et al., 2019). Sediment mass flux at each height $q(z)$ (kg m^{-2} s^{-1}) was calculated by:

$$q(z) = m \cdot A / T_s \tag{19}$$

where m is the mass of the sediment collected at height z, A is the area of the sampler inlet size (2.34×10^{-4} m^{-3}, and T_s is the sampling period. Exponential curves were fit to the data using nonlinear least squares regression of q on z using the form:

$$\widehat{q}(z) = q_0 e^{az+bz^2} \tag{20}$$

or

$$\widehat{q}(z) = q_0 e^{-az} \tag{21}$$

where q_0, a, and b are fitting parameters. Eq. (20) was used to fit the data if measurable sediment was collected at all heights. Eq. (21) was used if measurable sediment was collected at three heights. Data were excluded if measurable sediment was collected at two or fewer heights or if sediment weights did not decrease monotonically with height. Fits with

$R^2 < 0.80 \, or \ge 0.999$ were excluded from subsequent analyses. The upper limit was used to exclude samples that were overfit and produced unrealistic curves for heights other than the sample heights.

Q was calculated by integrating from $0 < z \le 1$ m:

$$Q = \int_0^1 \widehat{q}(z) dz \tag{22}$$

Following Webb et al. (2019), a natural log transformation was applied to Q and the spatial mean and variance were calculated for each observation period following Horvitz and Thompson (1952). The Horvitz-Thompson (HT) estimator of an unbiased mean $\overline{z}_{HT}$ for variable z for a stratified random sampling design is defined as:

$$\overline{z}_{HT} = \frac{\sum_{i=1}^{m} z_i / \pi_i}{n} \tag{23}$$

where π_i is the probability that the i th sample unit is included in the sample, m is the simple random sample set size within a stratum, n is the total sample size, and z_i is the value at sampling location i. The spatial variance of Q for each observation period was calculated as:

$$\widehat{V_s}(\overline{z}_{HT}) = \frac{\sum_{i=1}^{n} \left(\frac{1-\pi_i}{\pi_i} \right) X_i^2 + \sum_{i=1}^{n} \sum_{j \neq 1}^{n} \left(\frac{\pi_{ij} - \pi_i \pi_j}{\pi_i \pi_j} \right) X_i X_j}{n^2} \tag{24}$$

where π_{ij} is the inclusion probability of X_i and X_j population units being in the sample size (Horvitz and Thompson, 1952).

Model calibration was restricted to observation periods of Q that coincided with vegetation transect measurements at each site to best represent the influence of vegetation on parameter set likelihood (Table 2). For all included observation periods, vegetation transects were measured during or within two weeks of the beginning or end of the observation period. Observation periods were further parsed from the calibration data set if they included snowfall, heavy rainfall events, multiple rainfall events, or other circumstances that might interfere with reliable flux estimation. Hereafter, flux observations refer to the site-wide spatial mean fluxes calculated using Eq. (23).

Brief description of GLUE framework for model calibration

Transparently conveying the magnitude and sources of model uncertainty is critical for interpreting model estimates and using them to inform land management decisions. The GLUE model calibration framework was developed based on the premise of model equi-finality—i.e., there are many possible model structures and/or combinations of model parameters that are acceptable predictors of observed behavior (Beven and Binley, 1992). The other fundamental tenant of the GLUE framework is the explicit acknowledgment that sources and magnitudes of error—e.g., model structural error, measurement biases, observation methodology—and their relative contributions are
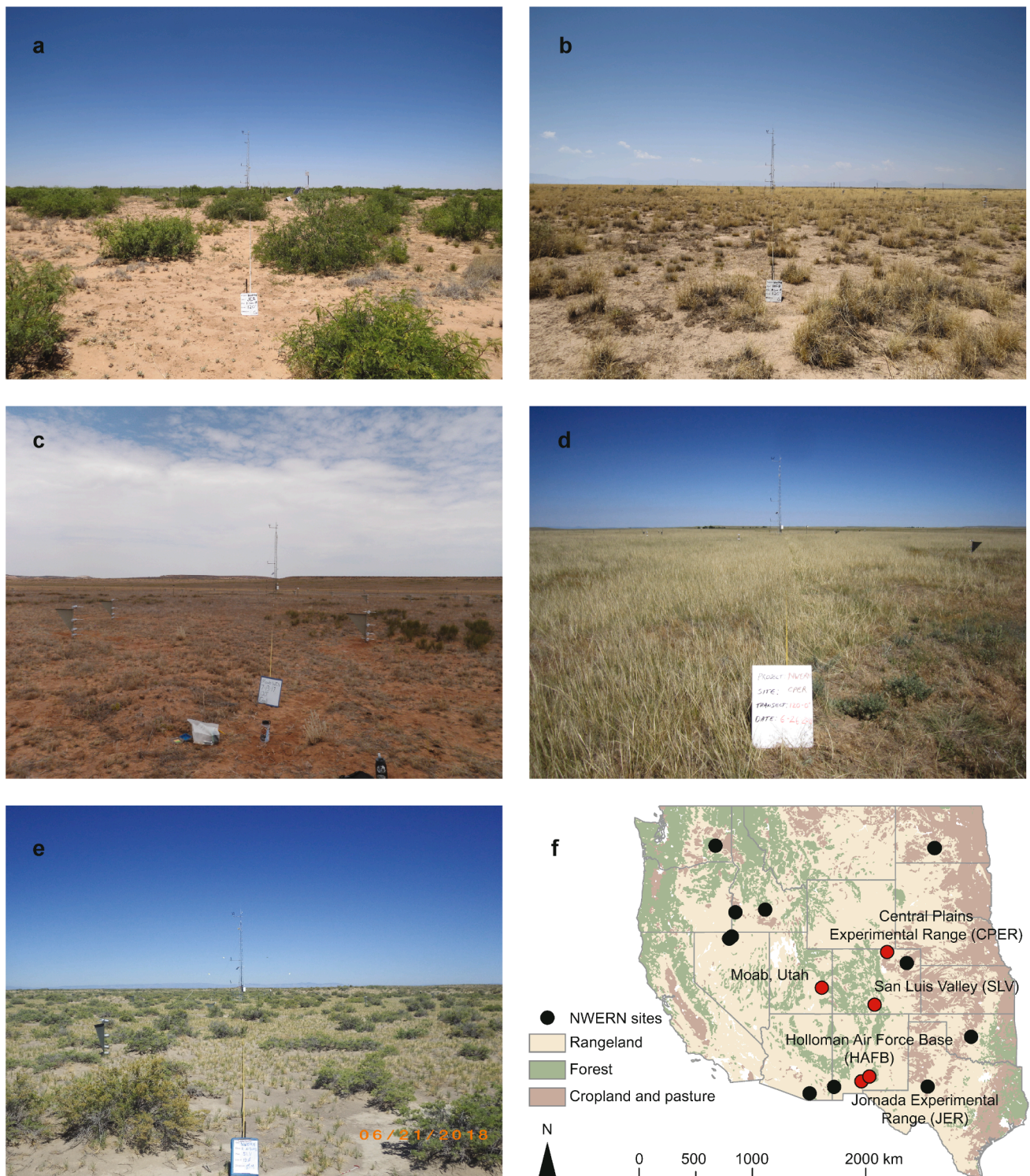
Fig. 2. Site photos taken along vegetation transects at a) JER, b) HAFB, c) Moab, d) CPER, and e) SLV National Wind Erosion Research Network (NWERN) sites; and f) location map of NWERN sites. Sites used in the current Aeolian EROsion (AERO) model calibration are highlighted in red. Sites indicated with black are cropland and rangeland sites that are currently being established or did not yet have sufficient observations and will be included in subsequent model parameterizations. Note: site in Manitoba, Canada not shown here. (For interpretation of the references to color in this figure legend, the reader is referred to the web version of this article.)

unknown (Beven and Binley, 2014). It also allows for future observations of the same or other variables to be added to model calibrations to improve performance or account for changing boundary conditions (Beven and Freer, 2001). The GLUE framework is particularly well suited to developing an aeolian transport model for application to land and resource management, given 1) the level of uncertainty in both

modeling and measurement of aeolian systems, and 2) the need for sediment flux estimates that represent the range of probable conditions over intermediate time scales (seasons to years), rather than a single estimate for a set of input forcing and boundary conditions. In addition, future calibration of the dust emission scheme can be easily incorporated with the horizontal flux calibration presented here, and model

Table 2

Spatial mean and variance of horizontal sediment flux (calculated using Horvitz and Thompson (1952) estimator) and vegetation transect information used to condition the Aeolian EROsion (AERO) model. Dates are the sediment flux sample collection dates at the end of ~ month-long sampling periods. *5-meter wind speeds were used because the 10-meter anemometer required maintenance.

Site	MWAC collection date	No. samples	Mean ln(Flux)	Variance ln(Flux)	Mean flux (gm^{-1} d^{-1})	Bare soil (%)	Mean vegetation height (m)
JER	21 Mar 16	25	3.03	0.52	20.74	0.69	0.26
JER	20 Apr 16	23	3.73	0.27	41.76	0.69	0.26
JER	13 Jul 16	22	2.67	0.51	14.43	0.68	0.25
JER	8 Mar 17	27	5.14	0.27	170.69	0.78	0.24
JER	5 Apr 17	27	4.52	0.26	91.74	0.78	0.24
JER	15 Nov 17	24	1.66	0.27	5.24	0.62	0.31
JER	20 Dec 17	14	−0.91	0.43	0.40	0.62	0.31
JER	14 Mar 18	24	2.64	0.76	14.07	0.71	0.30
JER	10 Apr 18	25	4.61	0.61	100.38	0.71	0.30
JER	6 Jun 18	26	2.62	0.74	13.77	0.69	0.33
JER	5 Jul 18	25	3.00	0.31	20.10	0.69	0.33
JER	26 Oct 18	23	2.15	0.26	8.59	0.71	0.30
JER	5 Mar 19	26	4.12	0.58	61.26	0.75	0.30
JER	4 Apr 19	25	5.73	0.26	306.95	0.75	0.30
HAFB	5 Nov 15	23	1.36	0.20	3.90	0.49	0.35
HAFB	28 Jul 16	22	2.17	0.03	8.74	0.54	0.24
HAFB	16 Nov 16	25	0.52	0.42	1.69	0.55	0.23
HAFB	5 Dec 17	15	−0.17	0.05	0.85	0.43	0.23
HAFB	28 Mar 18	21	2.61	0.01	13.66	0.48	0.52
HAFB	19 Jun 18	25	1.66	0.05	5.28	0.46	0.44
HAFB	17 Jul 18	24	1.80	0.02	6.03	0.46	0.44
HAFB	9 Oct 18	25	0.95	0.19	2.60	0.46	0.52
HAFB	7 Nov 18	22	0.36	0.86	1.43	0.46	0.52
HAFB	18 Mar 19	11	3.39	0.00	29.60	0.46	0.47
Moab	31 May 16	22	2.72	0.03	15.21	0.36	0.26
Moab	8 Nov 16	24	1.36	0.04	3.90	0.55	0.25
Moab	7 Dec 16	27	1.91	0.10	6.77	0.55	0.25
Moab	2 May 17	17	2.05	0.05	7.78	0.48	0.22
Moab	6 Jun 17	21	2.26	0.04	9.61	0.48	0.22
Moab	12 Oct 17	25	2.23	0.04	9.26	0.46	0.32
Moab	7 Nov 17	11	0.50	4.10	1.65	0.46	0.32
Moab	12 Jun 18	7	2.45	0.02	11.58	0.46	0.14
Moab	16 Aug 18	22	2.95	0.03	19.14	0.63	0.14
Moab	12 Dec 18	13	1.26	0.01	3.51	0.54	0.21
Moab	1 Apr 19	27	2.40	0.02	11.05	0.57	0.19
SLV	7 Jun 16	27	4.76	0.30	116.23	0.64	0.17
SLV	7 Sep 16	14	3.79	0.09	44.36	0.59	0.18
SLV	*8 Jun 17	26	3.65	0.24	38.34	0.58	0.18
SLV	*5 Jul 17	21	2.98	0.33	19.73	0.56	0.21
SLV	19 Oct 17	26	2.84	0.64	17.08	0.49	0.21
SLV	16 Jul 18	27	2.34	0.24	10.38	0.50	0.22
SLV	27 Sep 18	22	1.26	0.26	3.52	0.50	0.22
CPER	14 Jul 17	11	−0.70	0.12	0.50	0.12	0.49
CPER	14 Nov 17	8	−0.55	0.08	0.58	0.12	0.40

calibrations can be refined or purpose built for different environments (e.g., cropland) as suitable data become available. If desirable, subsequent sets of flux observations could also be included in the model calibration in such a manner that captures the transport system response to long-term environmental change, i.e., giving more weight to more recent observations (Beven and Freer, 2001).

The GLUE approach is conceptually straightforward but requires some subjective decisions prior to model calibration depending on specific goals (Beven and Binley, 2014). In short, a likelihood measure $L_T[M(\Theta|Y_T, Z_T)]$ based on the level of agreement between predictions and observations is calculated for model $M(\Theta)$ with parameter vector Θ conditioned on input vector Y and observation vector Z over some set of observations T. Many simulations—typically on the order of 10^3–10^6—are conducted using different model structures and/or parameter sets sampled from a specified prior distribution and results are compared to observations. Parameter sets are chosen independently, and no hypothesis about correlation structure is necessary in defining the prior distributions of the model parameters (Ratto et al., 2001). Thus, the likelihood surface is also independently sampled, and simulations can be weighted with minimal need for additional assumptions (Beven and Freer, 2001). A form of Bayes' equation can be applied, e.g., following Beven and Binley (1992), such that:

$$L[M(\Theta_i)] = L_0[M(\Theta_i)]L_T[M(\Theta_i|Y_T, Z_T)]/B \tag{25}$$

where $M(\Theta_i)$ is the ith model simulation, $L_0[M(\Theta_i)]$ is the specified prior likelihood of model $M(\Theta_i)$, and B is a scaling constant. Eq. (25) specifies the likelihood of the model structure and/or parameter set $M(\Theta_i)$ being correct, rather than the value of a prediction or the individual parameters being correct (Beven and Freer, 2001). $L_0[M(\Theta_i)]$ is either from the initial sampling of parameter space (typically from a uniform distribution of estimated parameter ranges) or from a previous model calibration. In such a way, the model calibration can be updated when new information becomes available.

GLUE implicitly accounts for unknown sources and structure of model error. The likelihood measure reflects the performance of a particular model—encapsulating errors associated with model structure, measurement or estimation of inputs, and measurement of observations. The likelihood measure also encapsulates covariation of parameter values on model performance (Beven and Freer, 2001). The exact form of the likelihood measure used to evaluate model performance must be chosen for the specific implementation. It can be based on traditional error models (e.g., Romanowicz et al., 1994, 1996), but typical forms include variations of the Nash and Sutcliffe efficiency criterion or a transformation of the model error variance:

$$\sigma_\epsilon^2 = \sum_i (\widehat{y}_i - y_i)^2 \tag{26}$$

where $\widehat{y}_i$ and y_i are modeled and observed values, respectively (Beven and Freer, 2001). The only requirement is that likelihood measures for each $M(\Theta)$ increase monotonically with the goodness of fit to observations $\mathbf{Z}$.

Each $M(\Theta)$ is then deemed an acceptable or unacceptable predictor of observations based on a predefined criterion of the likelihood measure. Unacceptable models are assigned a value of zero. Renormalization by B of acceptable models such that:

$$\sum_i L[M(\Theta_i)] = 1 \tag{27}$$

facilitates the calculation of prediction quantiles. Cumulative distributions of likelihood are constructed by ranking predictions from acceptable models and cumulatively summing the renormalized likelihood measures. Thus:

$$P(\widehat{Z}_t < z) = \sum_i L[M(\Theta_i) | \widehat{Z}_{t,i} < z] \tag{28}$$

where $\widehat{Z}_{t,i}$ is the value of the variable $\mathbf{Z}$ estimated for the observation at t by model $M(\Theta_i)$ (Beven and Freer, 2001). It is important to note that Eq. (28) is distinct for each observation—or time step, in most cases—against which the model is conditioned; hence the order of $M(\Theta_i)$ and shape of the cumulative distribution is distinct for each. Quantiles can then be calculated for a desired estimate of central tendency and level of uncertainty, e.g., the median prediction and 90% prediction bounds. In addition, probability distributions of predictions for individual observations can be examined, and marginal distributions of parameter values can be viewed qualitatively to assess model sensitivity.

Parameter space sampling and GLUE setup

Model parameter space was constructed from uniform distributions within reasonable estimated ranges of C, z_0, $\varphi_{\angle=0}$, r, and Γ (Table 3). The selected parameters represent either unmeasurable values or unknown parameters that relate models largely developed using data from limited, idealized experimental conditions to natural conditions. The use of uniform distributions simplifies parameter space sampling because no prior knowledge of the shape of the response surface is needed. Latin hypercube sampling was used to independently sample 10,000 parameter sets from the parameter space and model simulations were conducted.

The likelihood measure used to compare goodness of fit between simulation results and observations was calculated following Freer et al. (1996) as:

$$L_T[M(\Theta_i | \mathbf{Y}_T, \mathbf{Z}_T)] = e^{-N\sigma_{\epsilon i}} 2 / \sigma_{obs}^2 \tag{29}$$

where $\sigma_{\epsilon i}^2$ is the error variance for parameter set $M(\Theta_i)$ (i.e., Eq. (26)), N is a shaping factor, and σ_{obs}^2 is the variance of all observations used in the model calibration. Eq. (29) was chosen as the likelihood measure because equal weight is given to subsequent sets of additional observations when they are added to the model calibration. As such, when sufficient data become available from other rangeland sites to improve the model calibration, they can be included without disproportionately impacting the calibration. The shaping factor N determines the relative weight given to goodness of fit between simulations and observations in the likelihood surface. As N increases, increasingly higher likelihoods are assigned to the better simulations until eventually only the best is assigned a nonzero likelihood (Beven and Freer, 2001). Thus, the value of N influences the number of acceptable models and the peakedness of the resulting likelihood distribution. As such, the choice of N is subjective and determining an appropriate value may require some trial and error so that the distribution of acceptable model estimates is not too wide, yet most observations fall within prediction bounds. A value of $N = 3$ was used to calibrate AERO. Parameter sets resulting in likelihood values ≥ 0.3 were deemed acceptable for predicting sediment flux. Parameter sets with lower values were assigned a likelihood measure of zero.

Results

Site characteristics

Surface soil texture (top 1 cm) ranged from sandy loam to sand (USDA soil textural classes) at sites used to calibrate AERO. Mean and median grain sizes, respectively, for minimally dispersed PSDs were 211 and 169 μm at JER, 99 and 48 μm at HAFB, 150 and 110 μm at Moab, 241 and 191 μm at SLV, and 369 and 295 μm at CPER (Fig. 3). Both mean and median grain size were larger for the fully dispersed PSD for JER and SLV soils, increasing to 232 and 195 μm, and 251 and 202 μm, respectively. Mean and median grain size were smaller for the fully dispersed PSD for CPER, decreasing to 314 and 238 μm, respectively. Neither was appreciably different between the two PSDs for HAFB and Moab.

At JER, HAFB, and Moab, there was an increase in the frequency of particles between ~1 to ~60 μm and a corresponding decrease for larger particles between the minimally and fully dispersed PSDs resulting from aggregate dispersion. CPER soils showed the greatest difference between the two PSDs, with more finer particles for the fully dispersed PSD across the particle size range used in AERO. It should be noted that the laser particle size analyzer measures particle frequency up to 2000 μm, so this difference represents dispersion of large aggregates from 1000 to 2000 μm. The SLV soil is predominantly sand and there was negligible difference between the two PSDs although some minor disaggregation occurred, evidenced by the slight change in mean and median particle sizes.

The JER and SLV sites are classified here as shrublands and HAFB, Moab, and CPER as grasslands (Table 1, Fig. 2). Mean foliar cover over the period 2015–2019 ranged among sites from ~23% at JER to ~85% at CPER (Fig. 4a). Mean woody cover at both JER and SLV was ~10% and was ~2% or lower at HAFB, Moab, and CPER. Mean percent bare soil (E in Eq. (4)) ranged from ~3% at CPER to ~69% at JER (Table 3, Fig. 4c). Within-site variability in foliar cover and percent bare ground was highest at Moab and lowest at CPER, both grassland sites. CPER was
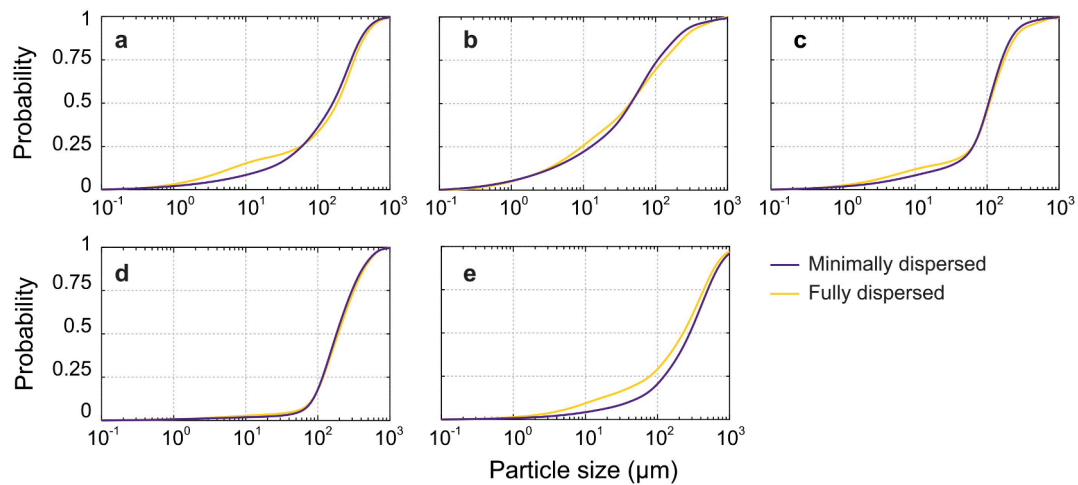
Table 3

Range of values of the prior (uniform) distributions of model parameters used to construct the parameter space for calibrating the Aeolian EROsion (AERO) model. Parameters are dimensionless unless otherwise noted. Q1, Q2, and Q3 are the quartiles of the marginal posterior distributions of model parameters following model calibration.

Parameter	Range	Basis for Estimated Limits	GLUE Q1	GLUE Q2	GLUE Q3	
C	0–0.5	Trial and error	0.03	0.06	0.10	
z_0 (m)	$\log_{10}(-4)$–$\log_{10}(-1)$	King et al., 2006; Marticorena et al., 2006; National Wind Erosion Research Network data; Ziegler et al., 2020	1.7	3.0	7.7	$\times 10^{-4}$
$\varphi_{\angle=0}$	0–0.5	Okin, 2008; Li et al., 2013	0.08	0.18	0.31	
r	2–8	Okin, 2008; Li et al., 2013	4.89	6.11	7.19	
Γ (kg s^{-2})	1.65–5 $\times 10^{-4}$	Shao and Lu, 2000	2.8	3.7	4.5	$\times 10^{-4}$

Fig. 3. Soil particle size cumulative distributions from the a) JER, b) HAFB, c) Moab, d) SLV, and e) CPER National Wind Erosion Research Network (NWERN) sites used to calibrate the Aeolian EROsion (AERO) model.
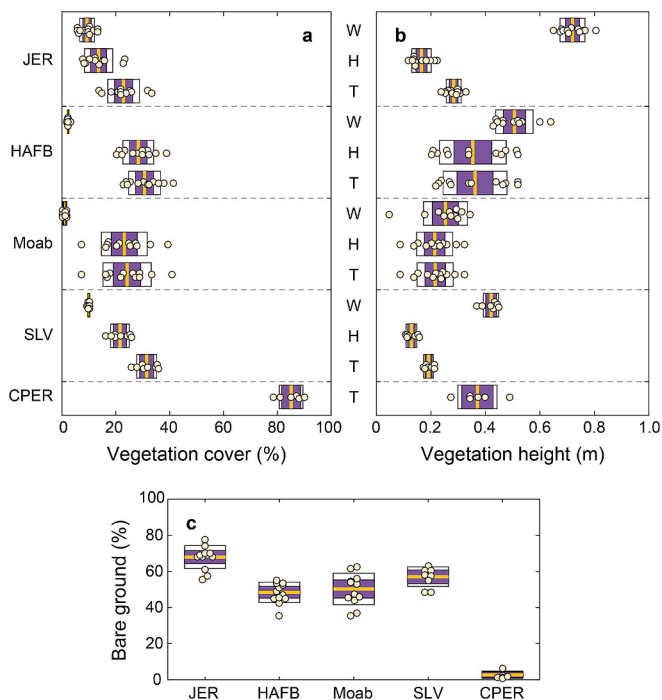

Fig. 4. a) vegetation cover, b) vegetation height and c) percent bare ground for all vegetation transect measurements to date for National Wind Erosion Research Network (NWERN) sites used to calibrate the Aeolian EROsion (AERO) model. Yellow lines indicate mean values, purple boxes indicate standard error of the mean, and white boxes indicate ± 1 standard deviation. Yellow circles indicate observations from individual transect measurements. W, H, and T stand for woody, herbaceous, and total, respectively. (For interpretation of the references to color in this figure legend, the reader is referred to the web version of this article.)

much more densely vegetated and exhibited less seasonal variability in cover. Foliar cover and bare soil were less variable overall at JER, HAFB, SLV than at Moab, but follow a similar pattern of variability in non-shrub cover, while shrub percent cover remained relatively stable. Percent bare soil for each observation period used to calibrate AERO is listed in Table 3.

Mean vegetation height for the period of record ranged from ~0.20 m at SLV to ~0.37 m at CPER (Fig. 4b). Within-site variability was highest at HAFB and lowest at SLV. Shrubs contributed significantly to

overall mean vegetation height and relatively low within-site variability in vegetation height for the two shrubland sites, JER and SLV. Between the two shrubland sites, mean shrub height was much higher at JER (~0.71 m) than SLV (~0.42 m). Mean non-woody vegetation height at the grassland sites was ~0.37 m, ~0.35 m, and ~0.21 m at SLV, HAFB, and Moab, respectively. Mean vegetation heights for the observation periods used to calibrate AERO are listed in Table 3.

For all sites, the highest proportion of unvegetated gaps was between 0.25 and 0.5 m, and there were few gaps larger than 3 m (Fig. 5). The general shape of the probability distribution of l_g was similar among sites and follows a typical gamma distribution, as suggested by Okin, (2008). SLV had the highest proportion of small unvegetated gaps, $l_g < 0.25$ m, and JER had the lowest. Within-site variability in l_g was highest for Moab and SLV and relatively low at other sites with the exception of the $0.25 < l_g \leq 0.5$ m range. Distributions of ℓ were similarly shaped to those for l_g with some minor differences following normalization by mean vegetation height, which varied among sites (Fig. 5b). The exception was CPER, where the frequency of ℓ skews noticeably to lower
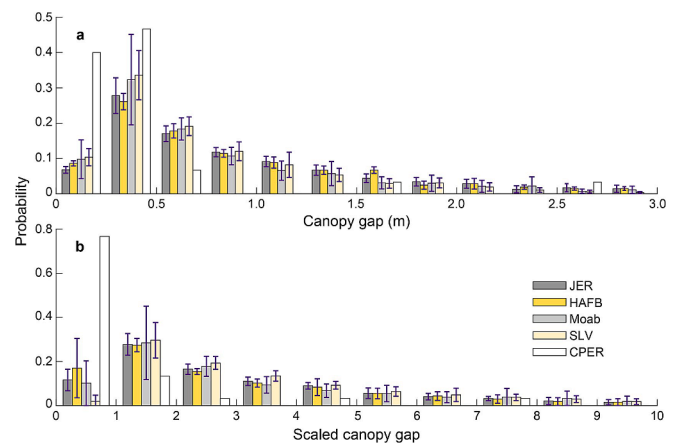
Fig. 5. Panel a) shows mean probabilities ± 1 standard deviation (purple bars) of on-the-ground canopy gap distances for all vegetation transect measurement dates for National Wind Erosion Research Network (NWERN) sites used to calibrate the Aeolian EROsion (AERO) model; and b) scaled canopy gap, calculated here as canopy gap distance divided by mean vegetation height. Bin width is 2.5 m and 1 (dimensionless) for canopy gap distance and scaled canopy gap, respectively. Standard deviations are not shown for CPER because only two observation periods were included in the model calibration. (For interpretation of the references to color in this figure legend, the reader is referred to the web version of this article.)

bins relative to l_g, which reflects dense vegetation cover where unvegetated gaps mostly comprise distances less than the canopy height.

Wind speeds during sediment flux observation periods are representative of both long-term and seasonal variability in meteorological conditions across the sites used to calibrate the model, except CPER, where observations periods did not capture the highest wind speeds during the period of record (Fig. 6). In general, for each site, periods with wind speeds approaching the maximum recorded during the period of record as well as periods characterized by relatively low wind speeds were used in the calibration. In addition, observations periods from spring, summer, fall, and winter were included for JER, HAFB, and Moab. For SLV and CPER, only summer and fall observation periods were included, largely because colder, wetter conditions and snow cover preclude sampling during winter and spring conditions. Mean daily wind speeds were highest at CPER ($\sim$4.6 m s^{-1}), followed by HAFB ($\sim$3.5 m s^{-1}), SLV ($\sim$3.4 m s^{-1}), JER ($\sim$3.2 m s^{-1}) and Moab ($\sim$3.0 m s^{-1}), respectively. CPER also had the largest variability in mean daily wind speeds over the period of record (standard deviation $\approx$ 1.9 m s^{-1}). Variability was similar at SLV, Moab, and JER (standard deviation $\approx$ 1.6, 1.5, 1.4 m s^{-1}, respectively), and lowest at HAFB (standard deviation $\approx$ 1.2 m s^{-1}). Maximum hourly wind speeds were similar for JER, HAFB, Moab, and SLV ($\sim$11.9, 10.8, 10.8, and 11.2 m s^{-1}, respectively) and

highest at CPER ($\sim$17.5 m s^{-1}).

Horizontal sediment flux observations

After eliminating horizontal sediment flux observations using the criteria described in Section "Parameter space sampling and GLUE setup", 44 observation periods across sites were selected to condition AERO flux predictions. Overall, the range of observed horizontal sediment fluxes across sites varied considerably, ranging several orders of magnitude (Fig. 7a; Table 3). Within-site variability was also large and spanned several orders of magnitude at all sites except CPER. These results indicate that the sites selected for calibrating AERO appropriately represent a large range of aeolian sediment transport rates that could be expected to occur in many rangelands.

AERO calculates fluxes using SI units, but hereafter fluxes are reported in g m^{-1} d^{-1}, which is a more meaningful unit given time frames of aeolian activity in rangelands (Li et al., 2013). Mean observed fluxes for the observation periods used to calibrate AERO were $\sim$65, 7, 9, 36, and 0.6 g m^{-1} d^{-1} at JER, HAFB, Moab, SLV, and CPER, respectively. Within-site mean fluxes were negligibly different for the entire period of record, and the across-site distribution of observations selected to condition the model calibration was comparable to the distribution of all observed fluxes (Fig. 7b). Thus, natural variability in sediment flux across a range of ecological conditions is encapsulated in the model calibration.

Model calibration

Model calibration resulted in 453 acceptable parameter sets. Uncertainty was estimated for 90% prediction bounds. Results show good agreement for individual sampling periods across sites, with most individual observations falling within prediction bounds (Fig. 8). Agreement was typically better for the largest flux values, and most of the observations that fell outside prediction bounds were for very small fluxes. For the entire set of observations, linear regression of the median GLUE predictions versus observations resulted in a slope $\approx$1 ($R^2 \approx 0.89$), with an RMSLE (root mean squared log error) $\approx$ 0.70 and RMSE $\approx$ 19 RMSE (g m^{-1} d^{-1}). These results indicate that the GLUE calibration setup—e. g., number of simulations, likelihood measure, prior distributions of parameters—was appropriate, and that AERO produces realistic estimates of Q across a range of rangeland vegetation and meteorological conditions.

It should be noted that for each observation used to calibrate the model—or subsequently, for each set of model inputs used to estimate flux for a specific plot or scenario— the GLUE methodology results in a
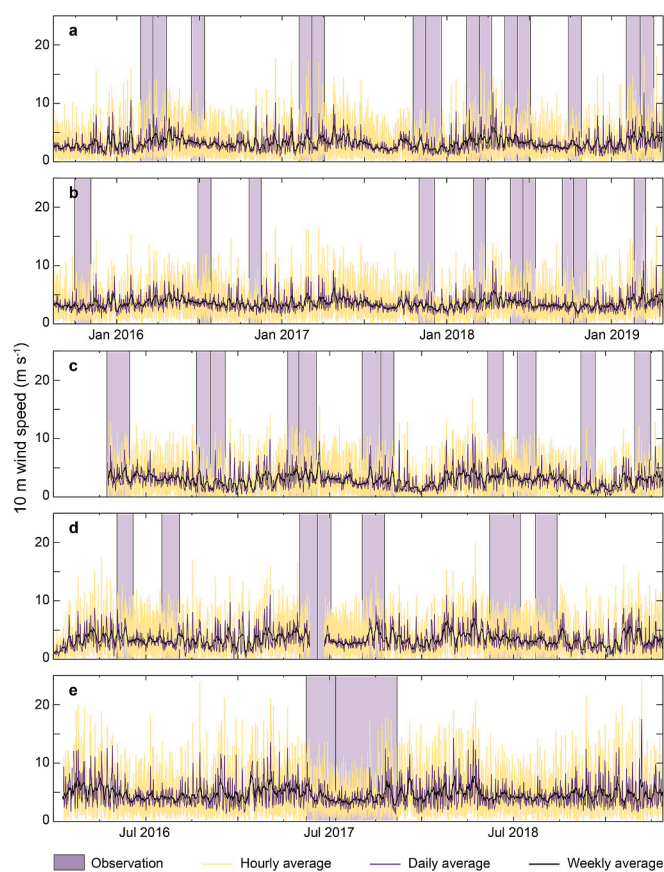

Fig. 6. Hourly, daily, and weekly 10-meter wind speeds measured at the a) JER, b) HAFB, c) Moab, d) SLV, and e) CPER National Wind Erosion Research Network (NWERN) sites. Note different periods of record, August 2015–April 2019 for JER and HAFB, January 2016–April 2019 for Moab, SLV and CPER. The light purple windows indicate the horizontal sediment flux observation periods used to condition the Aeolian EROsion (AERO) model calibration. Other than at CPER, observation periods are representative of both long term and seasonal variability in meteorological conditions across sites. Note missing 10-meter wind speed data in June and July 2017 at SLV. Five-meter wind speed data were used for model inputs for these observation periods. (For interpretation of the references to color in this figure legend, the reader is referred to the web version of this article.)
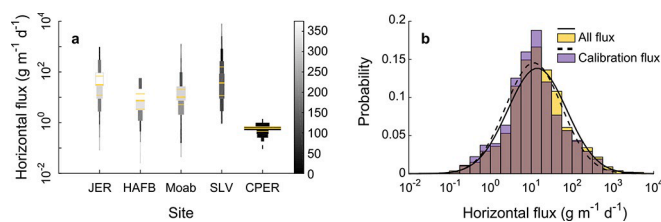

Fig. 7. a) Distribution plots of all observed horizontal sediment fluxes from National Wind Erosion Research Network (NWERN) sites used to calibrate the Aeolian EROsion (AERO) model. Color scale represents number of flux samples (27 per site per observation period) in each bin, and bin width represents relative density of points by bin for each site. Yellow lines indicate mean and standard error of the mean. b) Probability distributions (bin size = 0.25 in log10 space) for all horizontal sediment flux observations across sites and observations used to condition the AERO model calibration. As shown, the distribution of fluxes used for the calibration is representative of the distribution of all fluxes observed during the period of record across all sites (2015 through April 2019). (For interpretation of the references to color in this figure legend, the reader is referred to the web version of this article.)
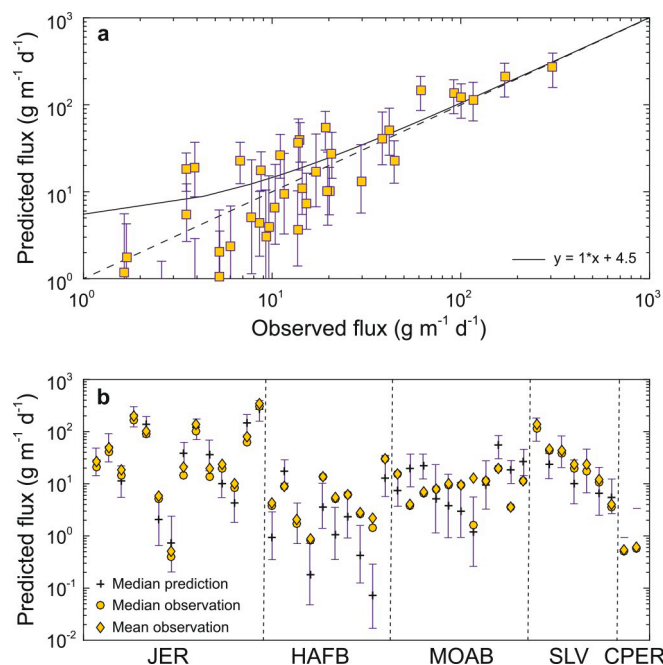
Fig. 8. a) Predicted versus observed horizontal sediment flux for the 44 observation periods used to condition the Aeolian EROsion (AERO) model calibration. Values shown are the median Generalized Likelihood Uncertainty Estimation (GLUE) predictions of flux and error bars are the 90% prediction bounds. Observed values are spatial means calculated using Eq. (23). Solid line is linear fit between predicted and observed flux and dotted line is 1 to 1. Notably, the slope of the relationship between median predicted and observed fluxes is 1 ($R^2 = 0.89$), indicating that choices made to construct the GLUE calibration framework, e.g., number of simulations, likelihood measure, prior distributions of parameters, were appropriate and that the AERO model successfully produces realistic estimates of horizontal sediment flux for rangelands. b) Median predicted flux for each observation period organized by site versus mean and median observed flux from the 27-mast MWAC array. Error bars are 90% prediction bounds. Notably, much of the disagreement between predicted and observed flux is for relatively low flux values.

unique probabilistic distribution of model predictions (Fig. 9). The ranked order of flux estimates from acceptable parameter sets is not necessarily the same across simulations because of the complexity of parameter interactions and relative influence of model inputs. The resulting distributions change in shape and variance across observations, and are thus non-Gaussian (Beven and Freer, 2001), highlighting limitations of using traditional statistical and optimization approaches based on the assumption that model errors are normally (or some other known form) distributed to parameterize complex environmental, including aeolian, models.

Marginal posterior distributions can be used to qualitatively assess model sensitivity to individual parameters and to approximate "best" values for individual parameters (Fig. 10). The median GLUE estimates of model parameters were ~0.061, 3.0×10^{-4}, 0.37×10^{-4}, 0.18, and 6.1 for C, z_0, Γ, $\varphi_{\ell=0}$, and r, respectively (Fig. 10, Table 3). The relative degree of departure from the prior uniform distributions used to construct the parameter space for parameter set sampling indicates the relative influence of the parameter on model simulation results and performance. The marginal posterior distributions for C and z_0 had the largest departure from the prior uniform distribution, indicating AERO is most sensitive to those parameters. The model appears least sensitive to Γ and $\varphi_{\ell=0}$. It should be noted, however, that some caution should be shown in interpreting these distributions, as the parameter sets as a whole are independent, rather than the individual parameter values (Beven and Freer, 2001).

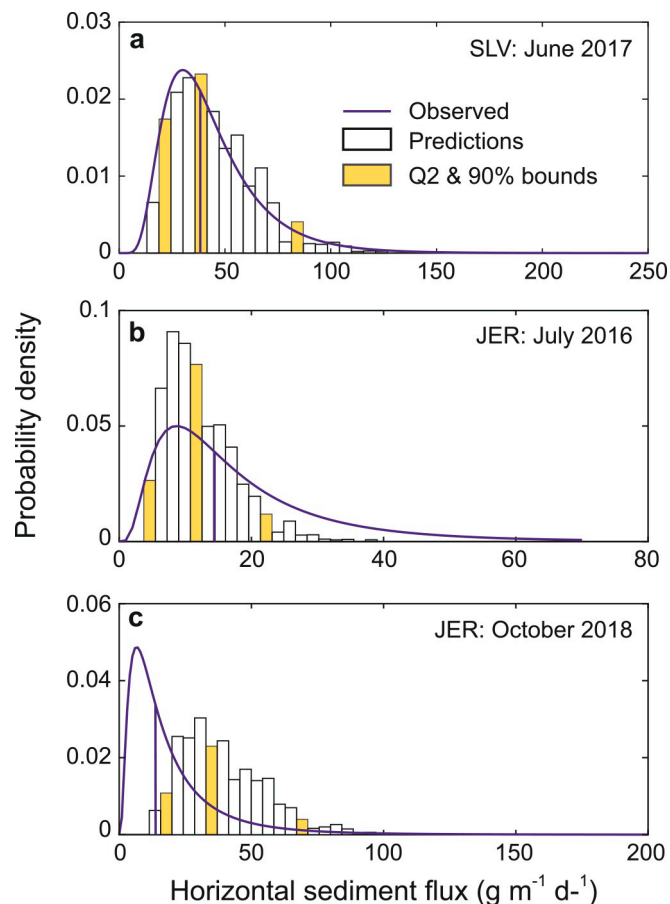On a site-by-site basis, the probability distribution resulting from

Fig. 9. Examples of probability density of horizontal sediment flux observations (from 27 Modified Cooke and Wilson (MWAC) samplers) and GLUE predictions (453 predictions binned into 20 bins) for a) an observation period with very good agreement between predicted and observed flux. Note the median prediction and mean observation overlap. b) an observation period with good agreement between observed and predicted flux. The median predicted and mean observed flux are not as close, but the observed mean is well within the 90% prediction uncertainty bounds and the distribution of predictions closely resembles observations. c) an observation period with poor agreement between observed and predicted flux, indicated by the spatial mean observed flux falling outside of the 90% prediction uncertainty bounds. Note that there is still significant overlap between observed and predicted flux in this case of poor agreement.

combining likelihood-weighted predictions for all observation periods at a given site more closely approximated the probability distribution of observations than for most single observation periods used to condition the model (Fig. 11). This approach—which can be interpreted as estimating the long-term distribution of aeolian sediment fluxes for a site—suggests that using a GLUE framework to condition an aeolian transport model encapsulates natural variability in transport rates resulting from time-variable vegetation and meteorological conditions and provides robust assessments of horizontal sediment flux probability suitable to inform land management. In particular, agreement between the long-term estimated and observed flux distributions was best for JER and SLV, which have the highest sediment transport rates among the sites used to condition the model. This outcome suggests that AERO more accurately predicts larger aeolian sediment transport rates that are likely to be of greatest significance for soil loss, dust emission, and feedbacks to ecosystem change (Bestelmeyer et al., 2018). Agreement between predictions and observations for both individual observation periods and the long-term flux distributions was poorest at HAFB. HAFB has a relatively high proportion of often strongly crusted gypsiferous soils, so it is possible that AERO overestimated flux at this site for
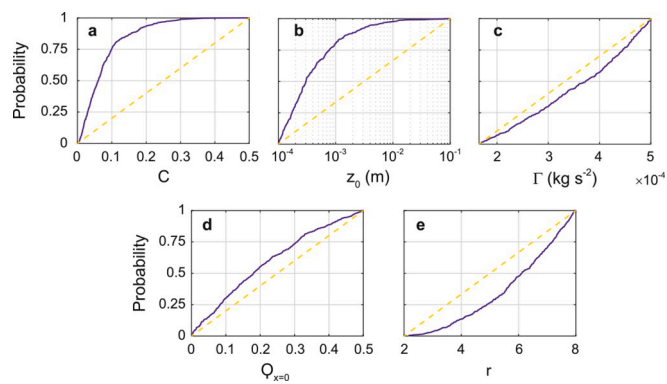
Fig. 10. Marginal posterior cumulative distributions of model parameters following calibration of the Aeolian EROsion (AERO) model for rangelands. Prior uniform distributions used to construct parameter space shown by dotted lines. Qualitatively, the level of departure of the marginal distribution away from the prior distribution indicates level of model sensitivity to each. Median values suggest a "best" value for each parameter, but it should be noted that the Generalized Likelihood Uncertainty Estimation (GLUE) framework relies on independence of parameter sets rather than individual values. Thus, while predictions using median parameter values for these marginal distributions will likely produce reasonable results, caution should be used in such an approach.
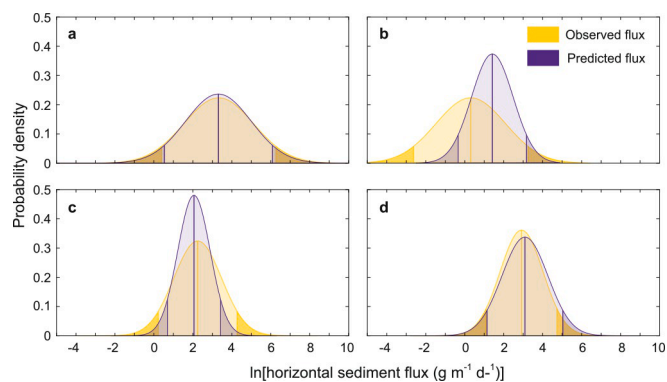
Fig. 11. Probability density of all observations (from all MWAC masts) of sediment flux during observation periods used to condition the Aeolian EROsion (AERO) model calibration compared to probability density of all likelihood weighted sediment flux predictions by site. Shaded tails are from the 0 to 5% quantile and from the 95% quantile to ∞, which represents the 90% prediction bounds for predicted flux. Plots are for a) JER, b) HAFB, c) Moab, and d) SLV National Wind Erosion Research Network (NWERN) sites. Data for the CPER site is not shown here because many of the observed and predicted fluxes are zero or negligible.

observed meteorological and vegetation conditions. In addition, particle density in Eq. (4) was adjusted to reflect the soil mineralogy at HAFB, but the saltation layer at the site often extends higher than for silicate soils. Because the MWAC masts were designed to integrate Q up to 1 m height, this precludes acceptable fits using Eq. (24) or Eq. (25) for many high transport periods. Thus, it is also possible that observed values of Q at HAFB are underestimated. These issues are also exacerbated by frequent influx of already entrained sediment to the site from the White Sands dune field, which is located ~5 km upwind. In either case, predictions and observations are still generally of the same order of magnitude, despite the relatively large disagreement in means compared to other sites.

Discussion

Overall, AERO produces realistic estimates of horizontal sediment mass flux distributions for varied rangeland vegetation and

meteorological conditions. Aeolian transport models are notoriously difficult to parameterize across multiple field observations, even from the same site or under near-ideal conditions (e.g., Sherman and Li, 2012; Sherman et al., 2013), because they often require site- and event-specific fits for parameter values. Moreover, at larger temporal and spatial scales, horizontal sediment flux and dust emission models often over-estimate aeolian transport rates by an order of magnitude or more (Haustein et al., 2015). We found the majority of AERO predictions were accurate within 90% prediction uncertainty bounds over several orders of magnitude of observed fluxes from five sites, with a linear regression slope of 1–1 (Fig. 8). These results suggest that while AERO is minimalist by design to accommodate standardized monitoring data (e.g., Toevs et al., 2011), the selected component schemes and overall model structure adequately describe the transport system over short to inter-mediate time scales (e.g., months to years) and a range of vegetation and meteorological conditions (Figs. 2–6). Perhaps more importantly from a management context, long-term probability distributions comprised of all flux predictions through time for a site agree very well with spatially distributed (27 MWAC sampler masts over a one-hectare site) observations over a period of several years, indicating that the GLUE model calibration approach sufficiently captures spatiotemporal variability in transport at these grassland and shrubland sites (Fig. 11). Agreement between long-term estimates and observations was particularly good for the two sites with the highest mean fluxes, which is promising for producing meaningful wind erosion estimates to inform management.

There are many reasons why process-based aeolian models are difficult to apply universally across diverse landscapes. Primary among them are 1) model development from limited experimental data (Sherman, 2020); 2) application of models that describe steady state, equilibrium conditions to represent processes that are more often than not intermittent across both space and time (e.g., Baas, 2008; Shao et al., 2020); 3) insufficient, or non-standardized observation sampling protocols (Webb et al., 2019; Sherman et al., 2018; Shao et al., 2020); and 4) the difficulty in representing spatially and temporally heterogeneous limiting factors on transport dynamics (e.g., Hagen, 2004; Namikas et al., 2010; Webb et al., 2021). These and other questions regarding uncertainties have persisted since the beginning of aeolian research as a discipline (e.g., Akiba, 1933; Cox et al., 1935), yet aeolian modeling remains an uncertain endeavor at best. Our basic understanding of the underlying physics has changed relatively little since early seminal works (e.g., Bagnold, 1936, 1941; Kawamura, 1951; and others), but the impact of uncertainty, including model structural errors, incomplete or unknown descriptions of processes, observational and measurement biases, and others remains largely unknown. For wind erosion and dust emission modeling, this has led to extensive model tuning (e.g., Ginoux et al., 2001; Zender et al., 2003) and application-specific (e.g., Tatarko et al., 2019) or region-specific approaches (e.g., Darmenova et al., 2009; Jarrah et al., 2020). Though these approaches work well under conditions or in geographies for which they were developed, they are difficult to generalize. Our aim with AERO was to develop a modeling approach that was generalizable across dryland systems, captured natural variability in transport rates, and communicated uncertainty in sediment transport predictions, which was accomplished by using a GLUE model calibration framework.

It should be noted that our application of GLUE methodology to AERO differs from the typical implementation. In most cases, GLUE is used to condition models with well-defined domains to time series observations, e.g., discharge from a specific catchment. We applied the methodology more generally to model a suite of processes at different locations, independent of time. The marginal posterior distributions of parameter values from acceptable models (Fig. 10) indicate that this approach reasonably encapsulates aeolian transport processes across distinct rangeland conditions. From a modeling standpoint, our results are also consistent with other recent research that suggests that parameter values for aeolian models should be treated stochastically because of the inherently variable nature of turbulent processes (Liu

et al., 2018). Median values and interquartile ranges (Table 3) of the posterior distributions are consistent with values of z_0, Γ, and r suggested in the literature (Shao and Lu, 2000; Okin, 2008; Li et al., 2013) or determined experimentally for a range of dryland environments (King et al., 2006; Marticorena et al., 2006), and for NWERN sites specifically (Ziegler et al., 2020). Median $\varphi_{\angle=0}$ is slightly lower than suggested by Okin (2008) and parameterized by Li et al. (2013), 0.18 versus 0.28–0.32, respectively, but seems reasonable given the mix of shrubland and grassland sites used in the model calibration. Values of C for acceptable parameter sets are much lower compared to values reported for equilibrium and near-equilibrium saltation conditions (e.g., Kawamura, 1951; White, 1979; Shao et al., 2011), but likely reflect the intermittent and supply-limited nature of saltation in sparsely vegetated drylands, and are of similar magnitude to values parameterized for similar environments by Li et al. (2013). Thus, AERO can be applied to rangelands generally without the need to reparametrize the model on a site-by-site basis. However, it should be noted the current model calibration may be limited for dissimilar dryland landscapes. While we included as many sites with suitable data as were available, and limiting factors such as soil crusting are inherently captured in the current calibration to the degree and duration they exist at the calibration sites, there is a great deal of diversity in vegetation cover and composition, surface soil characteristics, and meteorology not currently represented by the model. Ongoing work will extend the model calibration to incorporate data from disturbed rangeland sites (e.g., post-fire and brush management) and croplands under different management systems (e.g., conventional and no-till).

AERO can be used by land managers, government agencies, including transportation departments, and conservationists as a tool for adaptive management and planning. In this context, we foresee AERO to be used to: 1) assess aeolian sediment transport and dust emission rates; 2) identify conditions or actions that may lead to increased risk for soil erosion, blowing dust hazards, and degraded air quality; 3) assess effectiveness of conservation practices and whether management objectives are being met; 4) evaluate co-benefits and trade-offs for erosion management among ecosystem services; and 5) identify thresholds in vegetation cover and structure to avoid undesirable ecosystem state transitions and land degradation. In addition, the impact of a changing climate on rangelands globally remains uncertain, but some generalizations can be made about impacts to high level controls of wind erosion over the next few decades. Current projected trends in the western U.S., for example, are expected to cause regional shifts in vegetation cover and community composition; frequency, magnitude, and range of fire disturbance; and the frequency of high intensity, erosive weather events, all of which could lead to increased wind erosion and dust emissions in many areas (Edwards et al., 2019). Other available models largely fail to capture either short- or long-term variability in horizontal sediment transport or dust emission rates and are thus ill equipped to assess the potential impacts of gradual changes to forcing and boundary conditions through time. AERO simulations using climate change modelling scenarios could be useful in assessing wind erosion and dust emission response over seasonal to decadal time scales and in determining necessary land management changes, conservation treatment needs, and other actions that could be implemented now as a means to reduce estimated future risks.

For all cases, applications of AERO in these contexts will depend on the availability and/or capacity to collect needed input data, as well as the ability to interpret probabilistic estimates of aeolian sediment transport rates. Developing analysis frameworks and interpretive tools to provide context and benchmarks for assessing wind erosion and air quality will be important for users to apply erosion prediction tools like AERO to inform management (Webb et al., 2020b). To support interpretation, ongoing work seeks to build on an online version of the model that can run scenarios of land cover change, incorporate AERO estimates into land-potential (or site-specific) online databases of ecosystem dynamics (Bestelmeyer et al., 2016), and evaluate how quantitative

sediment transport predictions can complement qualitative and quantitative rangeland health assessment protocols (e.g., Pellant et al., 2018; Herrick et al., 2019).

Our approach to calibrating AERO also shows promise for other aeolian applications. Because the GLUE methodology accounts for equifinality, unknown biases, and structural errors among different models (Beven and Binley, 2014), a similar approach could be employed to what was presented here using both a suite of aeolian models and parameter sets. This could be a potentially useful approach to assess model performance in situations where different models, e.g., of saltation flux or threshold of motion, produce a wide range of results for the same inputs (e.g., Namikas and Sherman, 1995; Sherman et al., 1998; Edwards and Namikas, 2015). Our selection of specific equations (e.g., Kawamura, 1951) was based largely on straightforward integration with other model components. However, in the same way we used different parameter sets only to calibrate AERO, different model and parameter set combinations could also be used to calibrate models for other aeolian systems, effectively producing likelihood-weighted predictions constructed from the most accurate prediction ranges from a suite of models. In effect, the "best" part of each model would influence the overall result. Such an approach could improve, for example, sediment flux forecasting for beach and dune sediment budgets, where research has shown that different equations perform better for different conditions (Sherman et al., 2013).

Conclusions and future work

The AERO model was developed to provide rangeland managers with a tool to quantitatively assess wind erosion and dust emission. AERO leverages standardized ecosystem monitoring datasets to calculate probabilistic estimates of streamwise horizontal sediment mass flux, an indicator of soil and site stability, and size-resolved dust emission, an indicator of soil and nutrient loss and air quality. AERO balances the need for parsimony with process fidelity; the model can be applied using a minimum set of core inputs obtained in the field using standard monitoring methods (Herrick et al., 2018) or by remote sensing (e.g., Jones et al., 2018; Zhang et al., 2019; Zhou et al., 2020). AERO captures first-order controls to predict aeolian sediment transport across diverse soil types, vegetation communities, and land uses. Here, we have presented the AERO model structure and parameterization of the model threshold shear velocity, drag partition scheme, and horizontal mass flux equation for grassland and shrubland rangeland sites.

A Generalized Likelihood Uncertainty Estimation (GLUE) model calibration framework was used to parameterize horizontal sediment flux estimates for rangelands. Model calibration resulted in 453 acceptable models of horizontal aeolian sediment flux out of an initial 10,000 simulations. Median flux predictions exhibited a one-to-one relationship with observations of sediment flux. Long-term probability distributions of horizontal sediment flux predictions agree well with spatially distributed observations over a period of several years on a site-by-site basis, with agreement being best for the most active sites. AERO can be used by land managers, government agencies, and conservationists to assess potential aeolian sediment transport and dust emission rates for risk mitigation, determining the effectiveness of conservation practices, evaluating co-benefits and trade-offs for erosion management, and identifying critical thresholds in vegetation cover and structure for state transitions and land degradation. The next step in AERO development is to include parameterization of the vertical dust emission scheme in the model calibration when enough observations become available and continued refinement based on data from an increasingly large number of sites in the NWERN, representing an even greater diversity of conditions.

CRediT authorship contribution statement

Brandon L. Edwards: Conceptualization, Methodology, Software,

Validation, Formal analysis, Data curation, Visualization, Funding acquisition, Writing – original draft. **Nicholas P. Webb:** Conceptualization, Methodology, Software, Investigation, Resources, Funding acquisition, Project administration, Writing – original draft. **Magda S. Galloza:** Methodology, Software. **Justin W. Van Zee:** Conceptualization, Methodology, Investigation, Resources, Data curation, Supervision, Writing - review & editing. **Ericha M. Courtright:** Methodology, Software, Investigation, Data curation, Writing - review & editing. **Brad F. Cooper:** Investigation. **Loretta J. Metz:** Conceptualization, Writing - review & editing. **Jeffrey E. Herrick:** Conceptualization, Resources, Supervision, Funding acquisition, Writing - review & editing. **Gregory S. Okin:** Conceptualization, Methodology, Software, Writing - review & editing. **Michael C. Duniway:** Supervision, Investigation, Resources, Writing - review & editing. **John Tatarko:** Supervision, Investigation, Resources, Writing - review & editing. **Negussie H. Tedala:** Supervision, Investigation, Resources, Writing - review & editing. **Daniel N. Moriasi:** Supervision, Resources, Writing - review & editing. **Beth A. Newingham:** Supervision, Resources, Writing - review & editing. **Frederick B. Pierson:** Resources, Supervision. **David Toledo:** Investigation, Supervision, Resources, Writing - review & editing. **R. Scott Van Pelt:** Supervision, Investigation, Resources, Writing - review & editing.

Declaration of Competing Interest

The authors declare that they have no known competing financial interests or personal relationships that could have appeared to influence the work reported in this paper.

References

Achakulwisut, P., Shen, L.u., Mickley, L.J., 2017. What controls springtime fine dust variability in the western United States? Investigating the 2002–2015 increase in fine dust in the US Southwest. J. Geophys. Res.: Atmos. 122 (22), 12,449–12,467.

Akiba, M., 1933. The threshold wind speed of sand grains on a wetted sand surface. J. Agric. Eng. Jpn. 5, 157–174.

Alvarez, L.J., Epstein, H.E., Li, J., Okin, G.S., 2012. Aeolian process effects on vegetation communities in an arid grassland ecosystem. Ecol. Evol. 2 (4), 809–821.

Baas, A.C.W., 2008. Challenges in aeolian geomorphology: investigating aeolian streamers. Geomorphology 93 (1-2), 3–16.

Bagnold, R.A., 1936. The movement of desert sand. Proc. R. Soc. London. Ser. A-Math. Phys. Sci. 157 (892), 594–620.

Bagnold, R.A., 1941. In: The Physics of Blown Sand and Desert Dunes. Methuen, London, p. 265.

Bestelmeyer, B.T., Williamson, J.C., Talbot, C.J., Cates, G.W., Duniway, M.C., Brown, J. R., 2016. Improving the effectiveness of ecological site descriptions: general state-and-transition models and the ecosystem dynamics interpretive tool (EDIT). Rangelands 38 (6), 329–335.

Bestelmeyer, B.T., et al., 2018. The grassland–shrubland regime shift in the southwestern United States: misconceptions and their implications for management. BioScience 68 (9), 678–690.

Beven, K., Binley, A., 1992. The future of distributed models: model calibration and uncertainty prediction. Hydrol. Process. 6 (3), 279–298.

Beven, K., Binley, A., 2014. GLUE: 20 years on. Hydrol. Process. 28 (24), 5897–5918.

Beven, K., Freer, J., 2001. Equifinality, data assimilation, and uncertainty estimation in mechanistic modelling of complex environmental systems using the GLUE methodology. J. Hydrol. 249 (1-4), 11–29.

Cox, P., Sandford, K.S., Cornish, V., Spencer, L.J., Kitson, A.E., Bagnold, R.A., 1935. The movement of desert sand: discussion. Geogr. J. 85 (4), 365–369.

Darmenova, K., Sokolik, I.N., Shao, Y., Marticorena, B., Bergametti, G., 2009. Development of a physically based dust emission module within the Weather Research and Forecasting (WRF) model: assessment of dust emission parameterizations and input parameters for source regions in Central and East Asia. J. Geophys. Res.: Atmos. 114 (D14) https://doi.org/10.1029/2008JD011236.

Duniway, M.C., et al., 2019. Wind erosion and dust from US drylands: a review of causes, consequences, and solutions in a changing world. Ecosphere 10 (3), e02650.

Edwards, B.L., Namikas, S.L., 2015. Characterizing the sediment bed in terms of resistance to motion: toward an improved model of saltation thresholds for aeolian transport. Aeolian Res. 19, 123–128.

Edwards, B.L., Webb, N.P., Brown, D.P., Elias, E.H., Peck, D.E., Pierson Jr., F.B., Williams, C.J., Herrick, J.E., 2019. Climate change impacts on wind and water erosion on US rangelands. J. Soil Water Conserv. 74 (4), 405–418. https://doi.org/10.2489/jswc.74.4.405.

EPA, 2018. AP-42: Compilation of Air Emissions Factors. US Environmental Protection Agency.

Fécan, F., Marticorena, B., Bergametti, G., Marticorena, F., Bergametti, B., 1999. Parametrization of the increase of the aeolian erosion threshold wind friction velocity due to soil moisture for arid and semi-arid areas. Ann. Geophys. 17 (1), 149–157.

Freer, J., Beven, K., Ambroise, B., 1996. Bayesian estimation of uncertainty in runoff prediction and the value of data: an application of the GLUE approach. Water Resour. Res. 32 (7), 2161–2173.

Ginoux, P., et al., 2001. Sources and distributions of dust aerosols simulated with the GOCART model. J. Geophys. Res.: Atmos. 106 (D17), 20255–20273.

Gonzales, H.B., Casada, M.E., Hagen, L.J., Tatarko, J., Maghirang, R.G., 2017. Sand transport and abrasion within simulated standing vegetation. Trans. ASABE 60 (3), 791.

Goudie, A.S., 2014. Desert dust and human health disorders. Environ. Int. 63, 101–113.

Hagen, L.J., 2004. Evaluation of the wind erosion prediction system (WEPS) erosion submodelon cropland fields. Environ. Model. Softw. 19 (2), 171–176. https://doi.org/10.1016/S1364-8152(03)00119-1.

Haustein, K., Washington, R., King, J., Wiggs, G., Thomas, D.S.G., Eckardt, F.D., Bryant, R.G., Menut, L., 2015. Testing the performance of state-of-the-art dust emission schemes using DO4Models field data. Geosci. Model Dev. 8 (2), 341–362.

Herrick, J., et al., 2018. Monitoring manual for grassland, shrubland, and savanna ecosystems, volume 1: core methods. USDA–ARS Jornada Experimental Range Las Cruces, New Mexico.

Herrick, J.E., et al., 2010. National ecosystem assessments supported by scientific and local knowledge. Front. Ecol. Environ. 8 (8), 403–408.

Herrick, J.E., et al., 2019. A strategy for defining the reference for land health and degradation assessments. Ecol. Ind. 97, 225–230.

Horvitz, D.G., Thompson, D.J., 1952. A generalization of sampling without replacement from a finite universe. J. Am. Stat. Assoc. 47 (260), 663–685.

Jarrah, M., Mayel, S., Tatarko, J., Funk, R., Kuka, K., 2020. A review of wind erosion models: data requirements, processes, and validity. Catena 187, 104388. https://doi.org/10.1016/j.catena.2019.104388.

Jones, M.O., et al., 2018. Innovation in rangeland monitoring: annual, 30 m, plant functional type percent cover maps for US rangelands, 1984–2017. Ecosphere 9 (9), e02430.

Kachergis, E., et al., 2020. Guide to Using AIM and LMF Data in Land Health Evaluations and Authorizations of Permitted Uses. U.S. Department of the Interior, Bureau of Land Management, National Operations Center, Information and Publishing Services Section.

Kawamura, R., 1951. Study on sand movement by wind. Rept. Inst. Sci. Technol. 5, 95–112.

King, J., Nickling, W.G., Gillies, J.A., 2006. Aeolian shear stress ratio measurements within mesquite-dominated landscapes of the Chihuahuan Desert, New Mexico, USA. Geomorphology 82 (3-4), 229–244.

Kirchner, J.W., 2006. Getting the right answers for the right reasons: linking measurements, analyses, and models to advance the science of hydrology. Water Resour. Res. 42 (3) https://doi.org/10.1029/2005WR004362.

Li, J., et al., 2013. Evaluation of a new model of aeolian transport in the presence of vegetation. J. Geophys. Res. Earth Surf. 118 (1), 288–306.

Li, J., Okin, G.S., Tatarko, J., Webb, N.P., Herrick, J.E., 2014. Consistency of wind erosion assessments across land use and land cover types: a critical analysis. Aeolian Res. 15, 253–260.

Liu, D., Ishizuka, M., Mikami, M., Shao, Y., 2018. Turbulent characteristics of saltation and uncertainty of saltation model parameters. Atmos. Chem. Phys. 18 (10), 7595–7606.

Lu, H., Shao, Y., 1999. A new model for dust emission by saltation bombardment. J. Geophys. Res.: Atmos. 104 (D14), 16827–16842.

Lu, H., Shao, Y., 2001. Toward quantitative prediction of dust storms: an integrated wind erosion modelling system and its applications. Environ. Modell. Software 16 (3), 233–249.

Mahowald, N., et al., 2014. The size distribution of desert dust aerosols and its impact on the Earth system. Aeolian Res. 15, 53–71.

Marticorena, B., et al., 2006. Surface and aerodynamic roughness in arid and semiarid areas and their relation to radar backscatter coefficient. J. Geophys. Res. Earth Surf. 111 (F3), n/a–n/a.

Middleton, N.J., 2017. Desert dust hazards: A global review. Aeolian Res. 24, 53–63.

Namikas, S.L., Edwards, B.L., Bitton, M.C.A., Booth, J.L., Zhu, Y., 2010. Temporal and spatial variabilities in the surface moisture content of a fine-grained beach. Geomorphology 114 (3), 303–310.

Namikas, S.L., Sherman, D.J., 1995. A Review of the Effects of Surface Moisture Content on Aeolian Sand Transport. In: Tchakerian, V.P. (Ed.), Desert Aeolian Processes. Springer.

Okin, G.S., 2008. A new model of wind erosion in the presence of vegetation. J. Geophys. Res. Earth Surf. 113 (F2) https://doi.org/10.1029/2007JF000758.

Okin, G.S., et al., 2015. Connectivity in dryland landscapes: shifting concepts of spatial interactions. Front. Ecol. Environ. 13 (1), 20–27.

Parajuli, S.P., Stenchikov, G.L., Ukhov, A., Kim, H., 2019. Dust emission modeling using a new high-resolution dust source function in WRF-Chem with implications for air quality. J. Geophys. Res.: Atmos. 124 (17-18), 10109–10133.

Pellant, M., et al., 2020. Interpreting Indicators of Rangeland Health, Version 5: Bureau of Land Management Technical Reference 1734-6, Bureau of Land Management.

Pellant, M., Shaver, P.L., Pyke, D.A., Herrick J.E., Busby, F.E., Riegel, G., Lepak, N., Kachergis, E., Newingham, B.A., Toledo D., 2018. Interpreting Indicators of Rangeland Health, Version 5. Tech Ref 1734-6. U.S. Department of the Interior, Bureau of Land Management, National Operations Center, Denver, CO.

Pierre, C., et al., 2018. Impact of agropastoral management on wind erosion in Sahelian croplands. Land Degrad. Dev. 29 (3), 800–811.

Pimentel, D., et al., 1995. Environmental and economic costs of soil erosion and conservation benefits. Science 267 (5201), 1117–1123.

Ratto, M., Tarantola, S., Saltelli, A., 2001. Sensitivity analysis in model calibration: GSA-GLUE approach. Comput. Phys. Commun. 136 (3), 212–224.

Raupach, M.R., Gillette, D.A., Leys, J.F., 1993. The effect of roughness elements on wind erosion threshold. J. Geophys. Res.: Atmos. 98 (D2), 3023–3029.

Ravi, S., et al., 2011. Aeolian processes and the biosphere. Rev. Geophys. 49 (3) https://doi.org/10.1029/2010RG000328.

Romanowicz, R., Beven, K.J., Tawn, J., 1994. Evaluation of predictive uncertainty in non-linear hydrological models using a Bayesian approach. In: Barnett, V., Turkman, K.F. (Eds.), Statistics for the Environment II. Water Related Issues, Wiley, New York, pp. 297–317.

Romanowicz, R., Beven, K.J., Tawn, J., 1996. Bayesian calibration of flood inundation models. In: Anderson, M.G., Walling, D.E., Bates, P.D. (Eds.), Flood Plain Processes. Wiley, Chichester.

Schlesinger, W.H., et al., 1990. Biological feedbacks in global desertification. Science 247 (4946), 1043–1048.

Shao, Y., 2004. Simplification of a dust emission scheme and comparison with data. J. Geophys. Res.: Atmos. 109 (D10) https://doi.org/10.1029/2003JD004372.

Shao, Y., Ishizuka, M., Mikami, M., Leys, J.F., 2011. Parameterization of size-resolved dust emission and validation with measurements. J. Geophys. Res.: Atmos. 116 (D8) https://doi.org/10.1029/2010JD014527.

Shao, Y., Zhang, J., Ishizuka, M., Mikami, M., Leys, J., Huang, N., 2020. Dependency of particle size distribution at dust emission on friction velocity and atmospheric boundary-layer stability. Atmos. Chem. Phys. 20 (21), 12939–12953.

Shao, Y., Lu, H., 2000. A simple expression for wind erosion threshold friction velocity. J. Geophys. Res.: Atmos. 105 (D17), 22437–22443.

Sherman, D.J., Jackson, D.W.T., Namikas, S.L., Wang, J., 1998. Wind-blown sand on beaches: an evaluation of models. Geomorphology 22 (2), 113–133.

Sherman, D.J., 2020. Understanding wind-blown sand: six vexations. Geomorphology 366, 107193. https://doi.org/10.1016/j.geomorph.2020.107193.

Sherman, D.J., Li, B., 2012. Predicting aeolian sand transport rates: a reevaluation of models. Aeolian Res. 3 (4), 371–378.

Sherman, D.J., et al., 2013. Recalibrating aeolian sand transport models. Earth Surf. Proc. Land. 38 (2), 169–178.

Sherman, D.J., Li, B., Ellis, J.T., Swann, C., 2018. Intermittent aeolian saltation: a protocol for quantification. Geogr. Rev. 108 (2), 296–314.

Tatarko, J., Wagner, L., Fox, F., 2019. The wind erosion prediction system and its use in conservation planning. In: Bridging Among Discipl.ines by Synthesizing Soil and Plant Processes, pp. 71–101.

Toevs, G.R., Karl, J.W., Taylor, J.J., Spurrier, C.S., Karl, M, Bobo, M.R., Herrick, J.E., 2011. Consistent indicators and methods and a scalable sample design to meet assessment, inventory, and monitoring information needs across scales. Rangelands 33 (4), 14–20.

Webb, N.P., Chappell, A., Edwards, B.L., McCord, S.E., Van Zee, J.W., Cooper, B.F., Courtright, E.M., Duniway, M.C., Sharratt, B., Tedela, N., Toledo, D., 2019. Reducing sampling uncertainty in aeolian research to improve change detection. J. Geophys. Res. Earth Surf. 124 (6), 1366–1377.

Webb, N., Edwards, B., Pierre, C., 2020a. Wind erosion in anthropogenic environments. In: Reference Module in Earth Systems and Environmental Sciences. Elsevier. https://doi.org/10.1016/B978-0-12-818234-5.00031-6.

Webb, N.P., Herrick, J.E., Van Zee, J.W., Hugenholtz, C.H., Zobeck, T.M., Okin, G.S., 2015. Standard Methods for Wind Erosion Research and Model Development: Protocol for the National Wind Erosion Research Network. USDA-ARS Jornada Experimental Range, Las Cruces, USA.

Webb, N.P., et al., 2016. The National Wind Erosion Research Network: building a standardized long-term data resource for aeolian research, modeling and land management. Aeolian Res. 22, 23–36.

Webb, N.P., et al., 2020b. Indicators and benchmarks for wind erosion monitoring, assessment and management. Ecol. Ind. 110, 105881. https://doi.org/10.1016/j.ecolind.2019.105881.

Webb, N.P., et al., 2017. Land degradation and climate change: building climate resilience in agriculture. Front. Ecol. Environ. 15 (8), 450–459.

Webb, N.P., McGowan, H.A., 2009. Approaches to modelling land erodibility by wind. Prog. Phys. Geogr. 33 (5), 587–613.

Webb, N.P., McCord, S.E., Edwards, B.L., Herrick, J.E., Kachergis, E., Okin, G.S., Van Zee, J.W., 2021. Vegetation canopy gap size and height: critical indicators for wind Erosion monitoring and management. Rangeland Ecol. Manage. 76, 78–83.

White, B.R., 1979. Soil transport by wind on mars. Journal of Geophysical Research 84, 4643–4651. https://doi.org/10.1029/JB084iB09p04643.

Zender, C.S., Bian, H., Newman, D., 2003. The mineral Dust Entrainment And Deposition (DEAD) model: description and 1990s dust climatology. J. Geophys. Res. 108 (D14), 4416–4439.

Ziegler, N.P., Webb, N.P., Chappell, A., LeGrand, S.L., 2020. Scale invariance of albedo-based wind friction velocity. J. Geophys. Res.: Atmos. 125 (16) p.e2019JD031978.

Zhang, J., Okin, G.S., Zhou, B.o., 2019. Assimilating optical satellite remote sensing images and field data to predict surface indicators in the Western US: assessing error in satellite predictions based on large geographical datasets with the use of machine learning. Remote Sens. Environ. 233, 111382. https://doi.org/10.1016/j.rse.2019.111382.

Zhou, B.o., Okin, G.S., Zhang, J., 2020. Leveraging Google Earth Engine (GEE) and machine learning algorithms to incorporate in situ measurement from different times for rangelands monitoring. Remote Sens. Environ. 236, 111521. https://doi.org/10.1016/j.rse.2019.111521.